

PRINCETON UNIVERSITY

THESIS

A Stochastic Model of Cancer Cell Adhesion in Stokes Flow

Author:

Andre DOUGLAS

Supervisor(s):

Prof. Marcus HULTMARK

Prof. Winston SOBOYEJO

*A thesis submitted in fulfillment of the requirements
for the degree of Bachelor of Science in Engineering*

in the

Department of Mechanical and Aerospace Engineering

Fluid Mechanics Transport Phenomena Group

Soboyejo Group

April 27, 2016

Declaration of Authorship

I, Andre DOUGLAS, declare that this thesis titled, "A Stochastic Model of Cancer Cell Adhesion in Stokes Flow" and the work presented in it are my own. I confirm that:

- This work was done wholly or mainly while in candidature for a research degree at this University.
- Where any part of this thesis has previously been submitted for a degree or any other qualification at this University or any other institution, this has been clearly stated.
- Where I have consulted the published work of others, this is always clearly attributed.
- Where I have quoted from the work of others, the source is always given. With the exception of such quotations, this thesis is entirely my own work.
- I have acknowledged all main sources of help.
- Where the thesis is based on work done by myself jointly with others, I have made clear exactly what was done by others and what I have contributed myself.

Signed:

Date:

“Thanks to my solid academic training, today I can write hundreds of words on virtually any topic without possessing a shred of information, which is how I got a good job in journalism.”

Dave Barry

PRINCETON UNIVERSITY

Abstract

Marcus Hultmark

Department of Mechanical and Aerospace Engineering

Bachelor of Science in Engineering

A Stochastic Model of Cancer Cell Adhesion in Stokes Flow

by Andre DOUGLAS

In this work, a stochastic model that relates cell ratio(η), that is the ratio of cells that have adhesion sufficient to withstand the shear they are subjected normalized by the initial number of cells to the non-dimensional shear rate (γ^*) is developed. This model arises from a double-Gaussian fit of the rate of change of η with respect to γ^* which was obtained from experimental datasets. Using this model and coupling it with computational datasets from a prediction of the number of cells that exist with particular flow domains with prescribed initial conditions is obtained with a maximum error of 34%.

Acknowledgements

The author of this thesis is forever indebted to the following individuals for their insight, support and guidance that aided in the completion of this work.

Firstly, I would like to thank my advisors: Marcus Hultmark and Winston Sobojejo for their invaluable wisdom, knowledge and mentorship from conception to completion of this thesis. I would also like to thank the graduate students from Professor Hultmark's Fluid Mechanics Transport Phenomena (FMTP) Group: Matthew K. Fu and Clay E. Byers for their contributions to the development of the computational and theoretical models at the heart of this paper and also their assistance in the elucidation of experimental results. Also, I would like to thank Professor Michael E. Mueller for his great contribution to the completion of the computational portion of this thesis – including but not limited to the validation of the results of this code. I would also like to thank Professor Howard Stone for his deep and thoughtful insights into the fields over which this thesis presides.

I would also like to thank the members of Professor Sobojejo's group, in particular John Obayemi for his strong support during the experimental phases of this work. Special thanks also goes out to Mike Vucaturo for his assistance with the technical aspects of the experiment setup.

I'd also like to thank the Department of Mechanical Engineering at Princeton University in particular the curators of the John Marshall II Memorial Award Fund for providing a supportive environment where this research could have been conducted.

To my parents, my ever-present foundation, words cannot express how grateful I am to you for your calls, encouragement, support and love. I am forever indebted to you both.

I'd also like to thank my best friend Kevin Lopez, for helping me through the arduous process of writing, vetting, rewriting and developing coherent chapters for this thesis. You're the man KLo. *dab*

x

Last but not least, I'd like to thank the Heavenly Father for his support throughout this work. Especially in moments where results were scarce and the outlook was bleak, He kept me going.

Contents

Declaration of Authorship	iii
Abstract	vii
Acknowledgements	ix
1 Introduction	1
1.1 Introduction to the role of Fluid Mechanics and Material Science	1
1.2 Cell Adhesion to Surfaces	2
1.3 Introduction to Cancer	4
1.3.1 Trends In Cancer Mortality	5
1.4 Research Objectives and Summary	6
2 Literature Review	9
2.1 Theoretical and Experimental Review	9
2.2 Computational Review	22
3 Shear Assay Method for Cell Adhesion Measurement	27
3.1 Introduction to Cell Adhesion Measurement	27
3.2 Materials and Methods for Determining Cell Adhesion Strength and Characteristics	29
3.2.1 Materials and Substrate Preparation	29
3.2.2 Immunoflourescence Staining of Focal Adhesion	30
3.2.3 Shear Assay Measurements	30
3.2.4 Staining of Cells for Cell Counting	32
3.3 Protocol For Experimental Setup	32
3.3.1 Protocol For Laminar Flow to Create Shear Forces	32

Materials	32
Procedure	33
Protocol for Splitting/Passing Cells]	35
3.3.2 Protocol for Fixing Surfaces	36
4 Computational Evaluation of Domain	41
4.1 Computational Model Of Experimental Setup	41
4.2 Stability Analysis	44
4.3 CFD Results	46
4.3.1 MATLAB Code	48
4.3.2 C++ Code	50
4.4 Validation of Results with Commercial Code	60
5 Experimental Results and Discussion	63
5.1 Shear Assay Adhesion Results	64
5.1.1 Straight Channel Case	64
5.1.2 Backward Facing Step Case	71
5.2 Stochastic Model	73
6 Conclusion	79
6.1 Experimental and Numerical Conclusions	79
6.1.1 Ways to Improve the Numerics	79
6.1.2 Ways to Improve Experiments	80
6.2 Suggestions for Future Work	81
Bibliography	83

List of Figures

1.1	Schematic of Cell Adhesion to Biomaterials (Burridge, 1988)	2
1.2	Optical Image of Cells Stained to show Fibronectin Protein Filaments	3
1.3	Flow Features on backward Facing Step, (Rajasekaran, 2011)	7
2.1	Schematic of Vascular Shunt, Adopted from (Tannehill J, 2011)	13
2.2	Schematic of a cancer cell in the entry region of capillary with taper angle θ , upstream and downstream pressures P_1 and P_2 respectively, and a compression force normalized by area A_3 called the squeeze pressure, with A_1 and A_2 the upstream and downstream areas. Adopted from (Zeidman I., 1952) . . .	14
2.3	Plot of Adhesion and transit times versus separation distance, h_f . Adopted from (Weiss, 1989)	15
2.4	Schematic of cell undergoing ligand-mediated adhesion in the presence of flow adopted from(Weiss, 1989).	17
2.5	Free body diagram of cell undergoing mediated cell adhe- sion in the presence of viscous flow. Adopted from (Hammer DA, 1989).	19
3.1	Schematic of Parallel Plate Flow Chamber. Adopted from (Resto, V. A., 2008)	38
3.2	Shear Assay System Setup adopted from (Pins, G. D, 2006) .	38
3.3	Harvard Apparatus Syringe Pump with 50 ml syringes . .	39
3.4	Glycotech Parallel Plate Flow Chamber headers	39

4.1	Contour Plot of Streamlines in a 100×100 grid domain for $\text{Re} = 0.1$. This plot shows the initial state of the system at time, $t = 0$	46
4.2	Quiver plot of velocities in a 100×100 grid domain for $\text{Re} = 0.1$. This plot shows the initial state of the system at time, $t = 0$	46
4.3	Contour Plot of Streamlines in a 100×100 grid domain for $\text{Re} = 0.3$. This plot shows the state of the system at long time	46
4.4	Quiver Plot of velocities in a 100×100 grid domain for $\text{Re} = 0.3$. This plot shows the state of the system at long time	47
4.5	Contour Plot of Streamlines in a 100×100 grid domain for $\text{Re} = 0.6$. This plot shows the state of the system at long time	47
4.6	Quiver Plot of velocities in a 100×100 grid domain for $\text{Re} = 0.6$. This plot shows the state of the system at long time	47
4.7	Quiver Plot of velocities in a 100×100 grid domain for $\text{Re} = 1$. This plot shows the state of the system at long time	47
4.8	Quiver Plot of velocities in a 100×100 grid domain for $\text{Re} = 1$. This plot shows the state of the system at long time	47
4.9	Recirculation zone from FEM simulation on AutoDesk CFD Suite for Reynolds Number 0.3. Note the Similarity between this figure and figure 4.5.	60
5.1	Reynolds Number Dependence on No. Adhering Cells PDMS Channel - Straight	64
5.2	Reynolds Number Dependence on No. Adhering Cells PDMS Channel - Straight	65
5.3	Plot of the Cell Ratio η vs. shear stress γ^* for different viscosities, μ	67
5.4	Plot of the Cell Ratio η vs. non-dimensional shear rate γ^* for different viscosities, μ	67
5.5	Strain rate ($\dot{\epsilon}$) dependent viscoelastic behavior. Adopted from (Ozkaya, 2012)	70
5.6	Inclusion of Relaxation Time in Shear Rate Plot	70

5.7	Plot of the Cell Ratio η vs. non-dimensional shear rate γ^* for different viscosities, μ for the backward facing step case	71
5.8	Flow in the vicinity of the step. (a) $Re = 0.0001$, (b) $Re = 0.1$, (c) $Re = 10$, (d) $Re = 50$. Adopted from (G. Biswas, 2004)	72
5.9	Plot of $\frac{d\eta}{d\gamma^*}$ for different viscosities, μ	73
5.10	Plot of $\frac{d\eta}{d\gamma^*}$ for different viscosities, μ with fitted double-Gaussian curve. Mean of 0.7255 with Standard Deviation of 0.3702	74
5.11	Shear Rate Prediction for $Re = 1$	75
5.12	Corresponding η prediction using figure 5.10 and equation 5.5	76
5.13	Predicted Adhesion as a function of Shear Rate using Model and Numerical Simulation	77

List of Tables

2.1	Parametric Values of non-Newtonian constitutive equations	17
4.1	Validation Parameters	60
5.1	Flow Parameters of Various Blood Vessels	63
5.2	Natrosol viscosities by weight percentage in water at 35 C .	66

List of Abbreviations

ECM	Extra Cellular Matrix
EMT	Epithelial Mesenchymal Transition
CTC	Circulating Tumor Cell
Re	Reynolds Number
PDMS	Poly Di Methyl Siloxane
AFM	Atomic Force Microscopy

Physical Constants

Speed of Light $c_0 = 2.997\,924\,58 \times 10^8 \text{ m s}^{-1}$ (exact)

List of Symbols

l	distance	m
P	pressure	Pa
ω	vorticity	rad/s
ψ	stream function	
μ	dynamic viscosity	Pas
ρ	density	kg/m ³
u	x-directional velocity	ms ⁻¹
v	y-directional velocity	ms ⁻¹
τ	shear stress	Pa
γ	shear rate	s ⁻¹
N	number of cells	
N_0	initial number of cells	
η	Cell Ratio	
γ^*	Non-dimensional Shear Rate	

*Dedicated to Ayala and Nessa; who's love, laughter,
kindness and warmth still live on to this day...*

Chapter 1

Introduction

1.1 Introduction to the role of Fluid Mechanics and Material Science

The study of biological fluid mechanics tends to be a daunting one. However, with rapid progress being made in the fields of computational and experimental techniques in flow phenomena, we are more enabled to study and analyze more complex problems in fluid mechanics: that is, multiphase flows and flows over non-trivial geometries.

Recently a marked interest in the use of the techniques of fluid mechanics in problems such as surgical simulation, cancer metastasis studies and coronary artery disease progression gave birth to an exciting new subfield in fluid-mechanics known as Bio-fluids. With its advent comes an explosion of techniques to characterize the flow field around disease, which provides scientists with another tool to investigate the effectiveness of particular therapies and even observe disease progression present in interesting flow fields.

Coupled with the increased use of techniques in fluid mechanics in disease monitoring is the use of the methods in Material Science. Material Science, an equally broad discipline, which makes– from artificial heart valves and hip replacements to studies of cell elasticity being an indication of disease. In this study, however, the sector of Material Science that will be explored involves the measurement of cell-cell and cell-surface adhesion in particular morphologies, subjected to simple flows: channel flow and backward

facing step -both experimentally and computationally. These will be carried out first in the assumption of Newtonian regimes and then extended to non-Newtonian flows in future work.

1.2 Cell Adhesion to Surfaces

Considerations on cell-to-cell and cell-to-channel adhesions as previously mentioned is of great interest to the researcher. The cell-to-channel [more generally, cell-to-surface] interactions involve very complicated processes and have important applications for flow mediated response of cancer cell adhesion in flow. Cells adhere to the walls of channels [or in the high-level case to the walls of blood/lymph vessels] through the use of essential binding proteins (Mrksich, 2000).

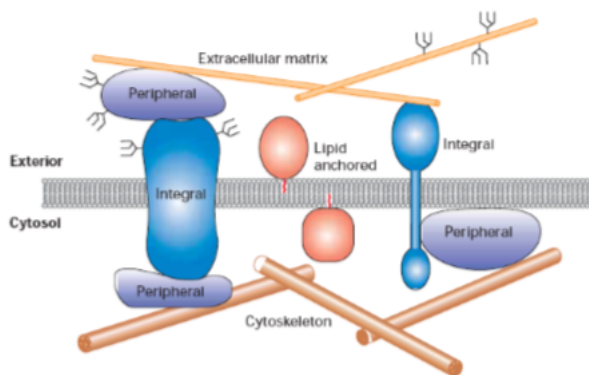


FIGURE 1.1: Schematic of Cell Adhesion to Biomaterials
(Burridge, 1988)

These proteins are secreted by cells in order to form the Extracellular Matrix (ECM) [as seen in figure 1.1]. The ECM matrix is comprised of an assortment of proteins and polysaccharides, mainly but not limited to collagen, Elastin, Laminin and Fibronectin (Alberts, 2002). These proteins are mainly manufactured and secreted in the Nucleus and shuttled to the Cell-Surface Membrane and then the material surface. They then organize themselves into a structured network that is closely associated with the outer surface morphology of the cell.

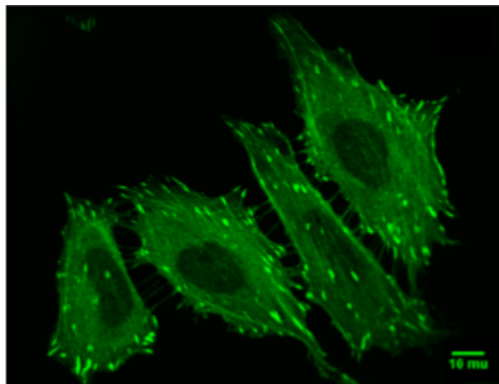


FIGURE 1.2: Optical Image of Cells Stained to show Fibronectin Protein Filaments

Many aspects of cellular behavior, including gene expression, signal transduction, apoptosis and motility are correlated to several surface properties such as roughness surface charge and surface free energy (Alberts, 2002). Studies have also indicated that both charge and wettability can influence the type, quantity and conformation of absorbed proteins. It is believed that surface proteins modulate cellular interactions through their effect on the composition of absorbed proteins. These proteins in turn mediate cellular adhesion (Ruoslahti, 1996).

Of particular importance to cell adhesion is the protein fibronectin [shown in figure 2]. The protein connects surface integrins [proteins which span the cell surface membrane] with collagen fibers in the ECM, causing a reorganization of the cell's cytoskeleton and facilitating cell movement on the ECM. Trans-membrane integrins, particularly the α and β subunits, are followed by an aggregation of receptors and an accumulation of intracellular proteins at the binding site. This leads to the formation of focal adhesions. Focal adhesion formation is characterized by the attachment of intracellular integrin components to intermediate proteins such as Vinculin and Talin, which in turn are connected to the cytoskeleton through bundles of Actin filaments known as stress fibers (Alberts, 2002, Ruoslahti, 1996).

Argine-Glycine-Aspartic acid (RGD) also has important functions in cell adhesion. The RGD sequence is a necessary cell adhesion peptide sequence, and is known to improve the tissue-material contact owing to high specific binding to cellular membrane integrin receptors (Auernheimer, 2006,

Senyah, 2005). Experiments have demonstrated increased focal adhesions on biomaterial surfaces fictionalized with biomimetic coating of RGD sequence.

Through the connection to cytoskeleton, focal contact exert a strong influence over cell spreading. Cell spreading is a complex process in which the cell creates extensions [more accurately: filopodia and lamellipodia] that contact the surface, form an adhesion and then exert a tension to create an outward motion of the cytoplasm (Friedl P, 2003a). Filopodia are long, finger-like extensions protruding from the cell, while lamellipodia are actin rich areas at the cell surface. This process is controlled by a sensitive balance of forces acting on the cytoskeleton. Tensional forces generated within cytoskeletal microfilaments tend to pull inward on the membrane, while focal adhesions resist these forces. In general, spreading results in a change of the shape from spherical to a flattened morphology with time.

Aspects of cellular behavior, such as gene expression, signal transduction, motility and apoptosis are also regulated by cell shape. Cell adhesion and spreading are parametrized strongly by cell shape (Raucher, 2000, Mitchison, 1996, Small, 1996). We may consider the a case of adhesion, circulating tumor cell arrest in metastasis and use these identifiable parameters as fundamental markers for characterizing this phenomena. Coupling this with particular flow regimes, the extent of adhesion can be used to "measure" and *identify* favorable environments for tumor cell attachment ie. particular regimes for increased affinity to certain cell-surface interaction.

1.3 Introduction to Cancer

Cancer has a major physical and emotional impact on society in the United States and the world. Indiscriminately, multiple forms of cancer target multiple systems of the body – often with deadly outcomes. According to the National Cancer Institute of the United States (Disease Control and Prevention, 2015).

1. In 2015 approximately two million new cases of cancer will be diagnosed in the United States alone. In the same time period, approximately 600000 people will perish from this disease.
2. Approximately 39.6 percent of men and women will be diagnosed with cancer during their lifetimes.
3. In 2014, approximately 16000 children and teens aged 0 - 19 were diagnosed with cancer and 12 percent of them died of the disease.
4. National expenditures on cancer care were 120 billion dollars in 2010 and are expected to increase by 24.8 percent to 156 billion dollars by 2020.

For comparison, according to the CDC, cancer kills annually more people than Chronic respiratory diseases, Accidents and unintentional injury, Strokes, Alzheimer's Disease and Diabetes combined. The only condition that harms more people per year is Heart Disease, placing cancer as the number two leading cause of death around the world.

1.3.1 Trends In Cancer Mortality

General trends in Cancer statistics are extremely concerning. New cases in cancer have remained constant over the year but its incidence is still at an alarmingly high number. The deaths due to cancer have also been fairly stable over the last 20 years. However, despite the advances in cancer research made during this time period, the death rate of cancer remains staggeringly high.

Biologically, two important intrinsic properties distinguish cancer cells from normal cells:

- Cancer cells can reproduce almost indefinitely in an uncontrolled manner.
- Cancer cells can invade and colonize surrounding, normal tissues by spreading to other locations through blood or lymph.

The process of metastasis is still not fully understood and the preference for particular regions of attachment have been noted in the literature but there is no conclusive theory to describe this observation (G. Biswas, 2004). Understanding metastasis, the most deadly stage of cancer, provides promising opportunities in predicting attachment points of circulating tumor cells and therefore concentrating treatment in these areas – somewhat of a cancer forecast system where disease tracking becomes more fine-tuned.

1.4 Research Objectives and Summary

This thesis presents an experimental and computational study of a two models of a blood vessel – a simple channel and a backward facing step, to determine if the flow features of localized vortices [as seen in figure 1.3] – characteristic of vascular shunts which punctuate the cardiovascular system, increases the likely hood for attachment of circulating cancer cells – either due to the vortex-induced repeated exposure of the cells to a surface or the *lower* shear stress environment present in these areas. These two morphologies were chosen because of the simplicity in their geometry which leads to easy analysis of the flow fields – at least in the Newtonian case. In addition to cancer cell arrest, this thesis also addresses key issues related to relationship between flow rheology and cell adhesion which are not well explored in the literature, including the relationship, if any, between shear stresses and shear rates on the likelihood of cell attachment.

Following the Introduction(Chapter 1) and literature Review (Chapter 2), this thesis is divided into two parts:

- An experimental treatment of the aforementioned morphology using the Shear Assay Device. The construction of the microfluidic channels and the arrangement of the apparatus to observe the adhesion of circulating tumor cells or conversely, the shear-removal of previously adhered cells.

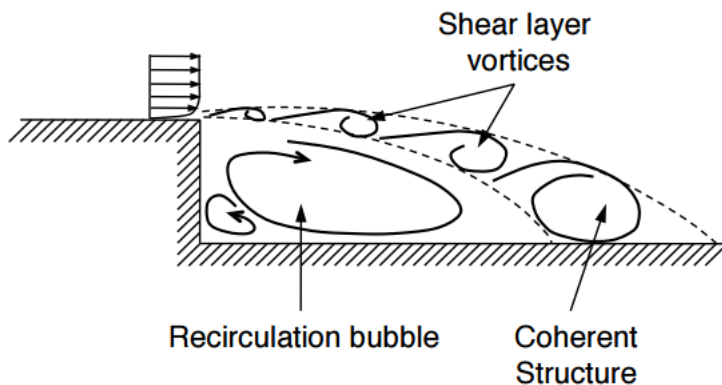


FIGURE 1.3: Flow Features on backward Facing Step, (Rajsekaran, 2011)

- Computational treatment of the same morphology in order to obtain flow parameters such as the shear stresses, reattachment point of the recirculation zone (in the case of the backward facing step) and shear rates being experienced near the walls of the device – as these are difficult to measure experimentally or theoretically predict.

Chapter 2 presents a review of the literature on flow mediated response of circulating tumor cells and fluid mechanical descriptions of tumor arrest conditions as well as crucial parameters such as shear stress. Adhesion force of tumor cells may be strong functions of these parameters, particularly under certain flow conditions.

Chapter 3 details the experimental method including the methods used to prepare the cells for shear, the setting up of the shear assay system: Glycotech's Parallel Flow Chamber with a Harvard Apparatus syringe pump. It presents a shear assay method for the measurement of cell-surface adhesion on selected biomaterials. The adhesion strengths between human cancer-cells (osteosarcoma) and biocompatible materials are investigated under shear flow. A combination of three-dimensional *in-situ* confocal image reconstruction. It also details the methods used to obtain the data: including counter staining of cells, the flow rate to match the required Reynolds Numbers.

Chapter 4 presents a finite difference, streamline vorticity solver for both flows, flow visualization comments on primary and secondary conservation of the solver, convergence in space and time and studies on the validity of the solution. This finite difference solver is also compared with a finite element fluid solver present in Autodesk Inventor's Simulation suite to provide validity to the results obtained.

Chapter 5 presents the results and discussion of the findings from the methods of chapter 4 when coupled with the results of chapter 3. Non-dimensionalization of parameters of interest and verification of correlations between these new parameters and parameters were care about such as the number of cells was also handled. The development of a new relationship that links cell adhesion to non-dimensional flow parameters is also carried out in this chapter. Salient conclusions arising from this work are presented in chapter 6 with suggestions of future work.

Chapter 2

Literature Review

2.1 Theoretical and Experimental Review

Cancer itself is one of the most dangerous diseases and it is more virulent at a particular stage—during metastasis. Metastasis is the process by which tumor cells migrate from the primary tumor location and form distant colonies in various organs. It is the primary reason for most cancer-related deaths (Pivkin, 2013). More than 90 percent of patients who die from cancer, perish because of the presence of satellite tumors and not simply due to the presence of the original tumor alone (Gupta GP, 2006, PS., 2006, Valastyan S., 2011). The reason why this is the case is due to ease at which an isolated tumor can be excised from a patient, in most cases, with the use of surgical techniques. With this in mind, it is obvious to see why the treatment of cancer post-metastasis is much less trivial.

Metastasis is biochemically and physically influenced and it is a complex, cascading multistep process in which migrant circulating tumor cells (CTCs) detach from the primary tumor, perforate the surrounding tissue and transport themselves through blood or lymphatic vessels (Gupta GP, 2006.) These CTCs then have the ability to proliferate while being transported attach to points within the circulatory systems of other (or the same) organs. Once attached, they begin to replicate the behavior of the primary tumor—they extravasate into the tissue, begin mass replication and support their rapid growth by the formation of new blood vessels through a process known as angiogenesis. All this culminates to the formation of a secondary, satellite

tumor.

Due to the complexity of the metastasis, its success is very dependent on the success of intermediate steps, any of which may be rate limiting and cascading to the final product (I.J., 2003). Interestingly, more than 99.99 % of the thousands of cells that enter the circulatory system during metastasis fail to produce a secondary tumor (Wirtz D, 2011) – that is metastasis has an efficiency of about 0.01 %. The detachment of carcinogenic cells from the original primary tumor is indicated by the process of epithelial-mesenchymal transition (EMT)) (Friedl P, 2003b and Polyak K, 2003), leading to considerable changes in the adhesive and mechanical properties (notably stiffness) of the tumor cells, making them more motile. Physiochemical processes are employed by these detached tumor cells to traverse the different microenvironments to reach the blood or lymphatic vessels (Labelle, 2011). Limited information is available on the exact mechanisms of the intravasation of tumor cells in blood vessels but it is proposed that the thinner, more damaged endothelium in the tumor microvasculature may provide migrating tumor cells with easy access to the circulatory system.

After entering the circulatory system, the transport of CTCs depends strongly on their physiochemical interactions with blood constituents and the wall vasculature as well as broader flow patterns. On the size of tumor cells, they are generally larger than Red Blood Cells (RBCs) and white blood cells. CTCs rarely circulate alone and are usually coupled through coagulation by platelets (Labelle, 2011). The resulting cell aggregates are some of the largest structures circulating inside the human vasculature and provide a double effect by protecting CTCs from immune cell recognition and reduces the shear stresses normally experienced by their unshielded, single circulating cancer cell counterparts (Gupta GP, 2006). The role of platelets is further complicated as studies show that platelets in direct contact with CTCs release a hormone called transforming growth factor Beta, which promotes the aforementioned EMT-like transition of CTCs (Sokolowski S,

1992). Platelets and the role of adhesion of CTCs and cancer cells thus plays a crucial role in cancer metastasis as it increases their motility, probability of survival in the circulation until their eventual arrest and extravasation at a secondary site. Platelet-CTC bodies disrupt blood flow, induce large forces on the endothelial cells (ECs), and result in large gradients of sheer along vascular walls (Sokolowski S, 1992).

Some studies have shown that in vivo and in vitro measurements of CTC flow velocities range from 3 to 12 mm/s (Sarimollaoglu M, 2011). This is 10 % slower than the corresponding mean blood flow velocity, with significantly slower velocities expected for CTCs that are on the order of the vessel diameter — that experience rolling along the surface of the vasculature. The interaction of the flow with the CTCs results in shear stresses as well as translational and rotational forces on them. Shear stress in vasculature range from 0.01 N/m^2 in capillaries to 4 N/m^2 in large arteries (Resnick N, 2003) where higher shear stresses may damage CTCs. Interestingly it is proposed that shear stress ranges may play a strong role in up-regulation of certain receptors and ligands (Struckhoff AP, 2010) that improve the potential of migrating CTCs to attach to the ECs of the vasculature. This may be analogous to interactions between white and red blood cells. During inflammation, the aggregation of RBCs in the center of blood vessels tend to push leukocytes (a type of white blood cell) toward the endothelial cells. Perhaps a similar processes occurs with CTCs but with a limited criteria for attachment relative to white blood cells.

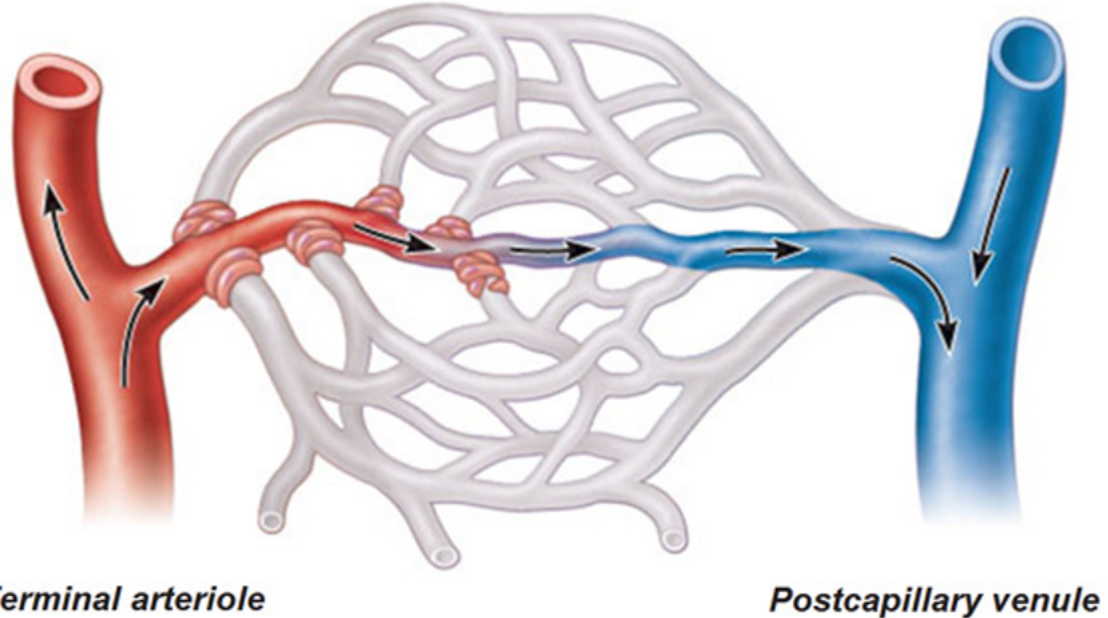
While the degenerate ultra-specificity of leukocytes enables them to recirculate until they find a suitable attachment site, CTCs instead appear to be transported by blood flow from primary intravasation location through the vasculature, to locations where they get trapped—usually in capillaries. The arrest of CTCs by capillaries depends on factors such as the relative size of CTC-platelet complexes, the blood pressure and the shear stresses in the capillary, and the deformability of the cells (Chambers A, 2002). To show

the strong dependence on vessel size, we see that as the vasculature carries blood from most tissues in the body through the heart and then to the lungs for oxygenation, the lung capillaries function as one of the major likely locations for trapping CTCs.

The lungs and liver are particularly adept at arresting CTCs (Chambers A, 2002) due to the small mean diameter of the capillaries (typically on the order of 3 – 8 micron) which carry a single red blood cell at a time, whereas cancer cells are considerably large (on the order of 20 micron or more in diameter) (Chambers A, 2002). Though it makes size of the tumor is a strong function of tumor arresting sites, it is good to note that not all tumor cells get trapped in the lung or liver capillaries, and some continue to circulate until they get trapped in other organs that are distant from the primary tumors. For example, Brain cancer cells have metastasized even to locations such as the femur bone marrow, located in the thigh, prostate tumors have been recorded to metastasize to the bones, and even two way metastasis between independent colonies have been observed in the breast and liver cancer cells (Hanahan D, 2011). Some CTCs evade arresting for notably long times as circulating breast cancer tumor cells have been detected in humans up to 22 years after successful treatment of the primary tumor(Meng S, 2004). Interestingly work by (Weiss, 1992) supports the argument proposed above. They claim that greater cell diameters, that is diameters of the CTC-platelet complexes, the less likely that they will be diverted from larger to smaller vessels and, it is more probable that they will pass directly through a vascular shunt.

A vascular shunt is a dynamic capillary network that is found in all organ systems. The capillaries in this network are guarded by sphincter muscles which can control the blood flow in the network. The proposition by Weiss could follow a mechanics where sphincter muscles sense the large size of the CTCs - complexes and contract to prevent these cells from gaining access to the capillary bed (Weiss, 1992).

Capillary Beds – “Vascular Shunt”



Terminal arteriole

Postcapillary venule

(b) Sphincters closed (sympathetic stimulation)—blood flows straight through Metarteriole Thoroughfare Channel and bypasses the true capillaries, “shunting” blood away from this area of tissue.

FIGURE 2.1: Schematic of Vascular Shunt, Adopted from
(Tannehill J, 2011)

Simplified models of cancer cell arrest have been developed with the help of concepts in fluid dynamics. By modeling the cells as smooth, viscoelastic spheres, moving along smooth-walled, fluid-filled tubes, where the floor is subject to a pressure gradient, a first order approximation can be obtained. Passage of cancer cells along capillaries is associated with the formation of a thin film of plasma separating them from the vascular endothelium. During passage, generated hydrodynamic forces in the plasma govern the passage of the cancer cell or its arrested state. When a cancer cell moves along a capillary wall, the rheologic properties of the plasma is a major contributor which regulates the contact between them (Weiss, 1992). Contact between the cell membrane and the vasculature can only be achieved by driving out the separating layer of plasma by pressure and shear forces. When the separation distance decreases below the cell radius, the pericellular hydrodynamic field will dominate motion (over the vascular flow field), slowing down the approach of the CTC to the vessel wall.

Deformability and motility of cancer cells is a prerequisite in order to enter capillaries due to the considerable difference in their diameters (Zeidman I., 1952). Because of this a number of local forces are present in this configuration outlined below:

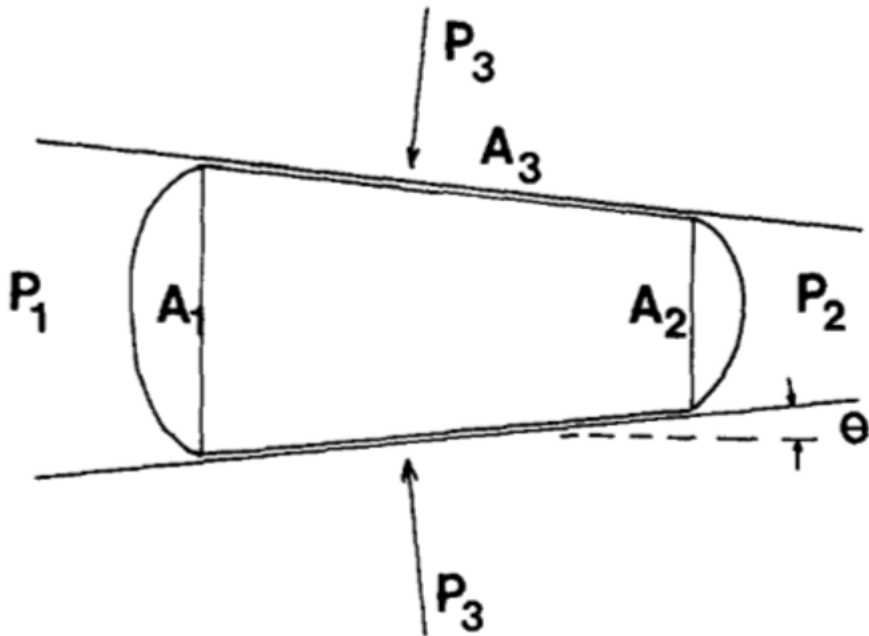


FIGURE 2.2: Schematic of a cancer cell in the entry region of capillary with taper angle θ , upstream and downstream pressures P_1 and P_2 respectively, and a compression force normalized by area A_3 called the squeeze pressure, with A_1 and A_2 the upstream and downstream areas. Adopted from (Zeidman I., 1952)

By a simple force balance we obtain that:

$$P_3 \sin \theta A_3 = P_1 A_1 - P_2 A_2 \quad (2.1)$$

With these local forces contributing the reduction in film thickness, a critical thickness of the film of plasma will then allow interactive forces (adhesion) to occur between the two sources, which if they are greater than the body forces on the cell due to blood pressure, will result in cancer cell arrest (Weiss, 1989).

With this in consideration, a comparison between the residence time and the adhesion time can be made. Given that this is low Reynolds number pressure driven flow, the velocity can be expressed as:

$$u = \frac{\Delta P h R \mu L}{2} \quad (2.2)$$

Where ΔP is the pressure difference across the cancer cell (on average ≈ 0.1 Pa), h is average film thickness (≈ 1 micron), R is capillary internal radius (≈ 2.6 micron), μ is plasma viscosity (≈ 0.2 pa sec), L is the length of cell opposed on vessel wall (≈ 40 microns). Considering this, a velocity of ≈ 0.1 cm/sec was obtained, and fixing the capillary length to 0.1 cm, gives a transit time of 1 s.

Writing adhesion time as equation 2.3 below, we obtain the following graph:

$$t = \frac{\mu R L^2}{2 T h_t^2} \quad (2.3)$$

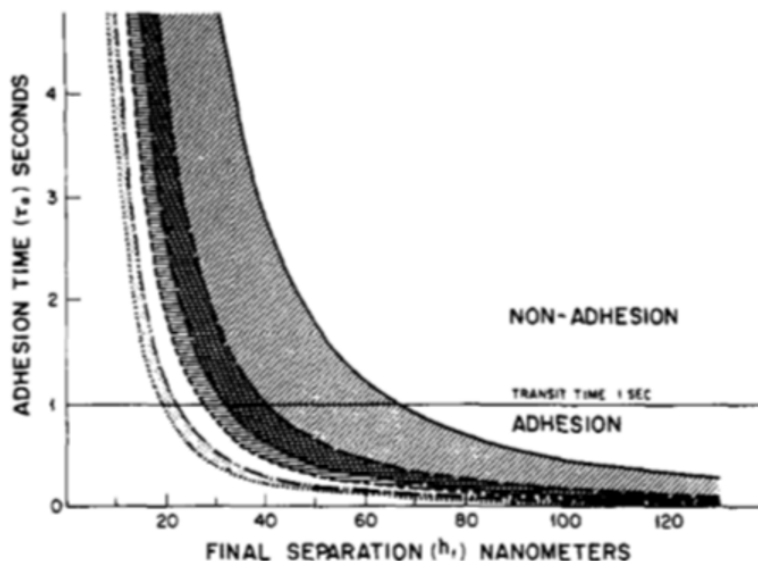


FIGURE 2.3: Plot of Adhesion and transit times versus separation distance, h_f . Adopted from (Weiss, 1989)

Where T is the effective mean tension of the cancer cell membrane and h_f is the film thickness. For a range of thicknesses from 0 to 120 nanometers shows that the adhesion times are much larger than the transit times for all

values of membrane tension when the film thickness is less than 20nm — the limiting case for attractive forces to be formed (Weiss, 1992).

However, since cancer cells have been observed being arrested by capillaries when the aforementioned criteria is not met, this model requires revision. One way that the experimenter may revise this is by considering that blood plasma is non-Newtonian or a generalized Newtonian fluid governed by the rheological equation:

$$\tau = \mu_e(\dot{\gamma})\dot{\gamma} \quad (2.4)$$

Where μ_e is the effective viscosity. The effective viscosity can now be modeled by power law, Casson Model or Carreau-Yasuda model (Collins W., 2005) where the power law is defined by:

$$\mu = k\dot{\gamma}^{n-1} \quad (2.5)$$

Where μ is the viscosity, k is flow consistency index and n the power law index which specifies the extent of non-Newtonian behavior. These indices are dependent on constituents of blood such as hematocrit etc (Collins W., 2005).

The Casson Model accounts for factors overlooked by the power-law model by consider that blood at rest requires some starting yield stress for flow. By appending this the following relation is obtained:

$$\mu = \frac{\tau_0}{\dot{\gamma}} + \sqrt{\frac{\eta\tau_0}{\dot{\gamma}}} + \eta \quad (2.6)$$

Where τ_0 is the yield stress and η is the Casson rheological constant. The values of τ_0 and η depends on hematocrit, H only (Hammer DA, 1989).

A third non-Newtonian model to consider is the Carreau model given by:

$$\mu = \mu_\infty + (\mu_0 - \mu_\infty)(1 + (\lambda\dot{\gamma})^2)^{\frac{n-1}{2}} \quad (2.7)$$

Where μ_0 and μ_∞ are the zero and infinite shear rate limit viscosities respectively, λ is the relaxation time constant and n is the power law index. The relaxation time and power law index shape the slope of the power law region. Given in table 2.1 are some typical values for the parameters stipulated in the above models (Collins W., 2005).

TABLE 2.1: Parametric Values of non-Newtonian constitutive equations

Parameters	Values
Flow Consistency Index (k)	0.017 Pa ⁿ
Power Law Index	0.708
Yield Stress, τ_0	0.005 N
Casson Rheological constant η	0.0035 Pa·s
Zero Shear rate limit μ_0	0.056 Pa·s
Infinite Shear rate limit μ_∞	0.0035 Pa·s
Relaxation time Constant λ	3.313 s
Power Law index in Carreau Model n	0.3568

Next we will consider the role of adhesion in the general sense and outside of the limited case of the aforementioned confined model, as presented in the frame of cell-mediated response presented by Hammer and Laufenburger (Hammer DA, 1989).

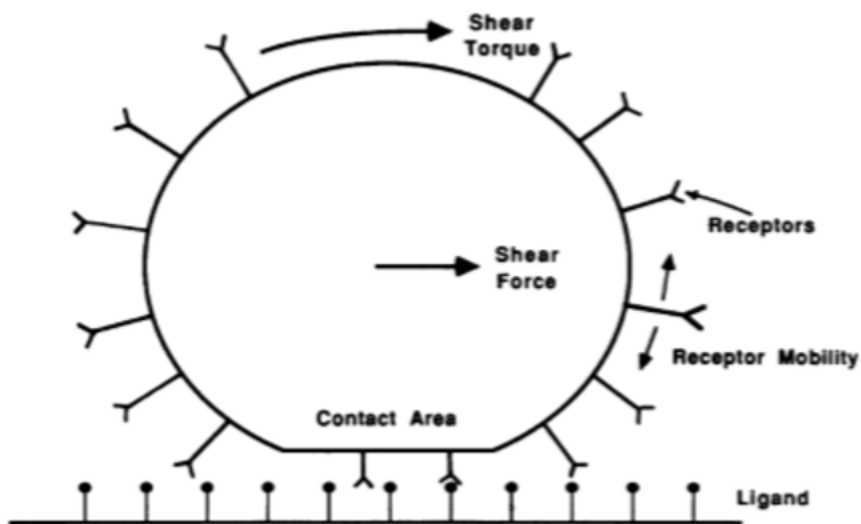


FIGURE 2.4: Schematic of cell undergoing ligand-mediated adhesion in the presence of flow adopted from(Weiss, 1989).

They consider several crucial quantities including: shear torque, shear force, receptor number, receptor mobility and contact area (Zeidman I., 1952). A number of simplifying assumptions are made to characterize the mathematical model:

- The cell possesses one receptor type of number R_T available for bonding. The contact area is assumed to be a disk of radius a . Receptors have an intrinsic mobility in the plane of the membrane, D .
- The contact area is well formed before molecular contact and this area remains constant throughout analysis due to small time scales of molecular interaction in adhesion.
- There is a short contact time, T_c , during which bonds can form between the cell and cell-surface ligands unstressed.
- The normal stress distribution can be approximated as constant over the contact area. This reduces stress dependence as a function of time and instantaneous space rather than position.

Considering these simplifications we obtain a series of differential equations characterizing the bond and receptor density:

$$\frac{dN_b}{dt} = k_f N_{l_0} N_a - k_r N_b \quad (2.8)$$

$$\frac{dN_a}{dt} = -k_f N_{l_0} N_a + k_r N_b + \Delta(N_{c_0} - N_a) \quad (2.9)$$

Where N_b is the bond density, N_a is the free receptor density, N_{l_0} is the ligand density on the substrate, k_f is the bond formation rate constant, k_r is the dissociation rate constant, N_{c_0} is the initial receptor density of the cell and Δ is the $1/t$ coefficient that accounts for accumulation of free receptors into the contact area — the mass transfer rate. The dissociation rate constant and mass transfer rate have different forms for different stress states: for unstressed ($t \leq T_c$) or stressed ($t > T_c$). When unstressed k_r may be written

as k_r^0 which is a constant (Hammer DA, 1989). When stressed k_r takes on the form:

$$k_r = k_r^0 e^{\frac{\gamma F_b}{k_b T}} \quad (2.10)$$

Where γ is characteristic length of bond, k_b is the Boltzmann constant, T is the absolute temperature and F_b is defined as the force per unit bond:

$$F_b = \frac{F_t}{\pi a^2 N_b} \quad (2.11)$$

Where F_t is the total force acting on the bonds and a is the radius of the contact area disk. To determine F_t the cell is assumed to be in mechanical equilibrium with fluid forces (Shear forces, F_s) and mechanical bond forces(F_b^x) in the x direction and torques due to the fluid forces:

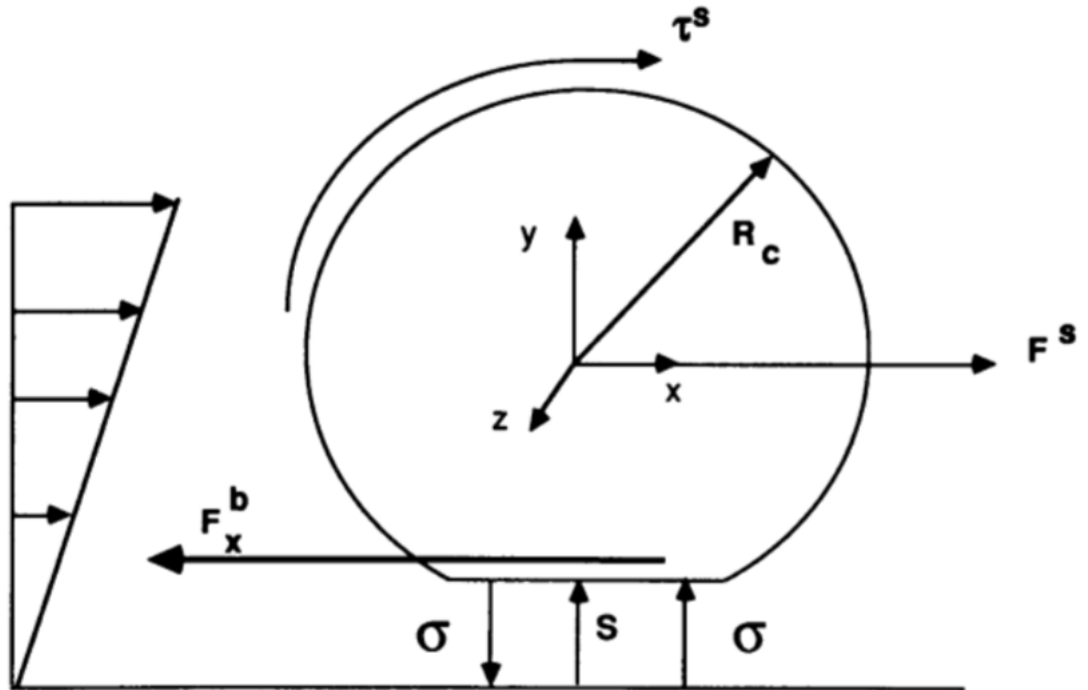


FIGURE 2.5: Free body diagram of cell undergoing mediated cell adhesion in the presence of viscous flow. Adopted from (Hammer DA, 1989).

$$0 = F_s + F_b^x \quad (2.12)$$

$$0 = \tau_s + F_b^x R_c + \int_0^{2\pi} \int_0^a \sigma N_b |r \cos \theta| r dr d\theta \quad (2.13)$$

here subscripts s and b represent shear and bonding and σ is the force per unit bond.

Solving each results in:

$$F_b^x = -F_s \quad (2.14)$$

$$F_b^y = -\frac{3\pi}{4a}(\tau_s + F_b^x R_c) \quad (2.15)$$

$$F_t = \sqrt{(F_b^x)^2 + (F_b^y)^2} \quad (2.16)$$

The forces and torques on a cell due in a viscous shear field are presented by (Goldman et al,1996):

$$F_s = 6\pi\mu R_c^2 \left(1 - \frac{S}{R_c}\right) \dot{\gamma} F^s \left(\frac{S}{R_c}\right) \quad (2.17)$$

$$\tau_s = 4\pi\mu R_c^3 \dot{\gamma} \tau^s \left(\frac{S}{R_c}\right) \quad (2.18)$$

In which F^s and τ^s are functions of dimensionless separating distance only. Combining all of this, an expression for the total force can be derived:

$$F_t = 6\pi\mu R_c^2 \dot{\gamma} \sqrt{\left(1 + \frac{S}{R_c}\right)^2 F^{s^2} \left(\frac{9\pi R_c^2}{16a^2} + 1\right) + \frac{3\pi^2 R_c^2}{4a^2} F^s \tau^s \left(1 + \frac{S}{R_c}\right) + \frac{\pi^2 R_c^2}{32a^2} \tau^{s^2}} \quad (2.19)$$

Where S is the separation distance. The transport rate constant. Δ , can be written as:

$$\Delta = \frac{2D}{a^2} + \frac{2\Omega R_c}{\pi a} \quad (2.20)$$

Where Ω is the angular velocity of the cell and for the conditions when the

bonds are stressed and the cell is not rotating $\Omega = 0$.

By non-dimensionalizing the parameters such that:

$$\tau = \frac{t}{T_c} \quad (2.21)$$

$$\eta_a = \frac{N_a}{N_{c_0}} \quad (2.22)$$

$$\eta_b = \frac{N_b}{N_{c_0}} \quad (2.23)$$

$$\theta = k_f N_{l_0} T_c \quad (2.24)$$

$$\beta = \frac{1}{4} \left(\frac{a}{R_c} \right)^2 \quad (2.25)$$

$$\kappa = \frac{k_f^0}{k_f N_{l_0}} \quad (2.26)$$

$$\alpha = \frac{\gamma F_t}{K_b T} \quad (2.27)$$

$$\delta = \frac{\Delta}{k_f N_{l_0}} \quad (2.28)$$

We obtain new equations for the model in terms of practical and important variables:

$$\frac{d\eta_b}{d\tau} = \theta \left[\eta_a - \kappa \eta_b \exp \left(\frac{\alpha}{\beta R_T \eta_b} \right) \right] \quad (2.29)$$

$$\frac{d\eta_a}{d\tau} = \theta \left[-\eta_a + \kappa \eta_b \exp \left(\frac{\alpha}{\beta R_T \eta_b} \right) + \delta(1 - \eta_b) \right] \quad (2.30)$$

Solving this system we are able to obtain explicit relationships between any parameter in the system and important parameters such as the dimensionless bond formation rate which determines when adhesion occurs. For full elucidation of this model, please consult Hammer DA, 1989

Interestingly this entire analysis was completed using an implicit Newtonian fluid assumption. To improve upon this model, non-Newtonian rheology (presented through equations 2.5 to 2.7) could be applied to better approximate the flow-adhesion relationship.

2.2 Computational Review

Most models in the realm of computational cancer therapy rely heavily on the principles of mass transport, in particular fluid mechanics. These computational models at the macroscopic scale are developed using mass balance equations for the cellular components, coupled with a system of convection-diffusion equations, for the concentration of extracellular chemicals, which can be written in the form (Bellomo N, 2008):

$$\frac{\partial(\rho_i \psi_i)}{\partial t} + \nabla \cdot (\rho_i \psi_i v_i) = \Gamma \quad (2.31)$$

$$\frac{\partial c_k}{\partial t} + \nabla \cdot (c_k v_l) = \nabla \cdot (Q_k \nabla c_k) + \Lambda_k \quad (2.32)$$

where ρ_i and ψ_i are the density and concentration of the i th cellular component (that is cells, extra-cellular fluid etc), v_l is the velocity vector of liquid (blood) and v_i is the mass velocity vector of the i th population, c_k are the concentrations of the k th nutrient. The Γ_i term in equation 2.31 represents both the source and sink term for each component, including cell death and cell birth. Tumor cells, particularly those engaging in adhesion constantly secrete chemical factors. In eq. 2.32 Q_k is the diffusion coefficient of the k th chemical factor and Λ_k is a source term for a particular nutrient. In other words, ψ_i is the volume fraction of the i th constituent, so the tumor is modelled as a multiphase material.

In order to close the systems of the equations, the velocity equation must be specified. For the case we are interested in, that is of low Reynolds number:

$$v_i = -D_i \nabla \psi_i \quad (2.33)$$

Where D_i is the diffusion coefficient. If this quantity is a positive constant, the cell movement will be described by linear diffusion (Sherratt JA, 2001).

As tumor cells grow and proliferate, they apply pressure to and perforate the surrounding tissue and the pressure, along with other mechanical interactions, have very crucial implications towards tumor cell adhesion and growth progression (Bellomo N, 2008). To restrict our computation discussion, we will refine the equations by considering blood flow in microvessels, whose diameters are on the order of 100 micron or less—aptly termed microcirculation (Sherratt JA, 2001). Microvessels have irregular spacial interconnections that form a network in tissues and are responsible for the exchange of materials between blood and surrounding tissues. Research on the flow through the neoplastic vasculature of solid tumors has been largely motivated by the desire to understand the role of fluid convection in the treatment of cancer by therapeutic monoclonal antibodies(Graziano L, 2007). A key problem in this kind of treatment is the low transport rates into the main body of the tumor across the vasculature, which leads to low and ineffective concentrations of the therapeutic macromolecules(Graner F, 1992). It is a common observation that interstitial fluid pressure is higher in both human and experimental solid tumors than in normal tissue. Enhanced interstitial pressure is the result of a highly permeable vascular network, combined with facilitated transendothelial fluid transfer. Clinically, a high interstitial pressure is marked by a reduced delivery and uptake of anticancer drugs (or macromolecules) and, hence, lack of therapeutic effects. Therefore, the analysis of blood flow and transport processes in the growing networks requires accurate modelling of blood flow in microvessels, solute transport, and angiogenesis (Collins W., 2005). Physically, blood is a suspension of red blood cells, white blood cells (leukocytes), and platelets in plasma. It is an incompressible Newtonian fluid with viscosity of about 1.2 cP at 37 C. Red blood cells are the most abundant, with a volume fraction of 40–45%, and therefore they strongly influence the rheology of blood. Because of their flexible viscoelastic membranes, they can easily pass through capillaries with diameters less than their major diameters at rest ($8\mu\text{m}$) (Graner F, 1992). In fact, the minimum diameter of a cylindrical tube that will allow a normal red cell to pass through intact is as narrow as $2.8\mu\text{m}$.

Leukocytes are generally spherical with a mean diameter of $6\text{--}8\mu\text{m}$ and are much less deformable than red cells. Despite their relatively small numbers, leukocytes can contribute significantly to blood flow resistance (Friedl P, 2003a). The rheological properties of blood flowing in microvessels have been extensively studied by in vitro experiments, using a suspension of red cells flowing through capillary tubes (Gossett DR, 2012).

Accurate numerical simulations of blood flow in microvessels must certainly include detailed models of blood cells as well as the glycocalyx layer attached to the endothelial surface. The dimensional irregularities of vessel diameters is another important factor (Erbertseder K, 2012). The Reynolds number of the blood flow in microvessels is «1, so that in general non-linear convective acceleration terms ($\nabla \cdot (\nabla v)$)in the momentum balance equations describing the plasma flow and the cell motion can be neglected (Fedosov DA, 2012). Since the plasma is known to be an incompressible Newtonian fluid, its motion is governed by the Navier-Stokes equations:

$$\rho \frac{\partial v}{\partial t} = -\nabla p + \mu \nabla^2 v \quad (2.34)$$

along with the continuity equation:

$$\nabla \cdot v = 0 \quad (2.35)$$

where v is the velocity vector, p is the pressure, ρ is the density, and μ is the dynamic viscosity of the plasma. Early simulations aimed at modelling the flow of red cells in narrow tubes under axisymmetry, the flow fields around cells and shear stress on the cell membrane, and flow resistance due to irregularities of vessel lumen as well as the effects of glycocalyx and leukocytes are reviewed in Sugihara-Seki and Fu (2005), and described in full detail in the references therein (Fedosov DA, 2012). Notably lower shear regions

were marked at points of divergent or convergent flow for simulated vessels (Sugihara-Seki M, 2005). More recent simulations using continuum-based models [similar to streamline vorticity methods] have shown that coupling of solid components and fluid flow in these models poses a number of challenging problems. For example, computational complexity can be attenuated by coupling discrete models of red cells with mesoscopic methods for flow discretization such as the lattice Boltzmann method, multi-particle collisional dynamics, and dissipative particle dynamics. Numerical simulations have indicated that the effect of leukocyte and cancer cell adhesion to the vessel walls on flow depends strongly on the number of adherent leukocytes and the vessel diameter. Owing to many similarities in the process of leukocyte and circulating tumour cell adhesion, models developed for leukocytes can also be applied to circulating tumour cells during the metastasis process (Auernheimer, 2006, Fedosov DA, 2012 and Gossett DR, 2012). Microvessel walls consist mainly of endothelial cells. Vascular endothelium is the principle barrier to, and regulator of, material exchange between circulating blood and the body tissues. The ultrastructural pathways and mechanisms whereby endothelial cells and the cleft between the cells modulate microvessel permeability to water and solutes have been a classical question in microvessel transport since the early 1950s (MB, 1996). If capillary walls act like semi-permeable membranes, fluid motion across them depends on the net imbalance between the osmotic absorption pressure of the plasma proteins and the capillary hydraulic pressure generated by the heart beating. Most existing models of transport through the inter-endothelial clefts are based on continuum approaches (Stephanou A, 2006). However, it was suggested that more suitable analyses should be based on the molecular nature of the fluid because of the sizes of the mean inter-molecular distances (0.3 nm) and the cleft width (18 nm) (Styp-Rekowska B, 2011). The development of multiscale computational models, coupling, for example, the molecular structure of the glycocalyx with a continuum description of the flow, is highly suitable in this context. Moreover, solute

transport from the vasculature to the cells has been largely modelled as passively transported elements with a flux proportional to the drug concentration. Solute transport inside the tumour was recently analyzed using computational models of diffusion based on high-resolution images (Sugihara-Seki M, 2005).

Chapter 3

Shear Assay Method for Cell Adhesion Measurement

3.1 Introduction to Cell Adhesion Measurement

The adhesion between biological cells is of high importance for many biological processes: from the integration of biomedical implants to cancer metastasis. Cancer metastasis which involves the spreading of detached cancer cells which travel to new regions of the body to form colonies rely on adhesion to establish contact with endothelial cells of the organs in which they are arrested.

Due to significance of cell-surface adhesion, a number of researchers have developed different techniques for the measurements of cell adhesion, as discussed in Chapter 2. The Atomic Force Microscopy (AFM) measurement of cell adhesion, measurements of adhesion can obtain extremely small [down to sub-pico-Newton] magnitudes of accuracy for specific ligand receptor interactions – some of which were reviewed in Chapter 2 (Gossett DR, 2012).

Other technique, such as optical tweezers and micropipette methods have also been widely used to also measure the adhesion strength. However, all of these methods result in *hard* contacts with cells – physical contact between measuring device and the cell surface membrane. This interferes with cells *in situ* and thus may illicit additional biological responses in the cell (Erbertseder K, 2012).

Compared to the *hard* contact methods, hydrodynamic forces exerted by fluid flow *softly* detach cells from surfaces, and are less likely to induce additional biological responses that may interfere with the measured strength data. Centrifugation and rotating planes have also been used widely to measure the adhesion strength. However, the *in-situ* observations of living cells are difficult during such measurements (Erbertseder K, 2012, Fedosov DA, 2012). Parallel flow chambers seem like the optimal case as it enables the measurements of the onset of cell detachment which can be monitored with microscopy.

Generally, cell detachment stress during shear assay measurements have been measured using simple models of the boundary layer equations that only account for the wall shear stress. However, this does not adequately account for the cell shape, which is crucial when analyzing circulating tumor cells (MB, 1996). As a result, computational scientists, DiMillia and Goldstein developed numerical simulations to simulate the effects of cell shape on the detachment of murine 3T3 fibroblasts from self-assembled monolayers (Stephanou A, 2006). These simulations involved the numerical solving of the 3-d Navier stokes equation and demonstrated that cell shape should be considered in modeling of fluid flows over cells (Zhang, 2003).

Using the adhesion of circulating Leukocyte as a template, we may use similarity to predict the adhesion behavior of circulating tumor cells to the vascular endothelium in shear flow environments. Circulating leukocytes bind to the wall by adhesion molecules, and show a characteristic *stop-and-go* motion of rolling(Ruoslahti, 1996, Styp-Rekowska B, 2011 and Stephanou A, 2006). Increasing attention has been placed on the morphology of Leukocytes as they adhere, the characteristic *tear drop* shape, which presents itself during shear flow. When compared to a rigid spherical form, there is increasing evidence that the *tear-drop* shape may significantly reduce the shear stress and fluid drag acting on the leukocytes and hence increases the lifetime of the Selectin bonds (Sugihara-Seki M, 2005).

Consequently, cell shape plays a key part in accurately estimating flow resistance and fluid drag and then understanding the mechanics of cell adhesion in the micro-environment around cells (Sugihara-Seki M, 2005, Friedl P, 2003a, Bowers V.M., 1989, Gossett DR, 2012).

Shear stresses also a crucial role in the deformation of cytoskeleton filaments and the concentration of focal adhesions. The effects of shear stress have been elucidated for the binding between integrin and the ECM (Bowers V.M., 1989). Those studies have demonstrated that the global activation of shear forces by fluid flow is transported to the local focal adhesion locations of cells (Guo, 2006). Thus, there is a need to determine the relationship between adhesion strength measured by shear flow and the connection between overall adhesion strength and the detailed cellular focal adhesion (Chu, 1994). The cells chosen for this experiment were Human Ovarian Carcinoma A2780 obtained from Sigma Aldrich (RPM 1-1640 + 2mM Glutamine + 10% foetal Bovine Serum).

3.2 Materials and Methods for Determining Cell Adhesion Strength and Characteristics

3.2.1 Materials and Substrate Preparation

The primary material used in this experiment included polished acrylic and poly-di-methyl-siloxane [PDMS]. This PDMS was made by mixing 10 parts of 184 silicone elastomer(Dow Corning, Germantown, WI) base with one part of curing agent. After fully stirring, the mixed solution was put under house vacuum for approximately 20 minutes to remove the small air bubbles to developed during the stirring process. The mixture is then cured at 60deg C for 12 hours. Regular cleaning process with deionized water and 100 % ethanol was used before cell culture.

3.2.2 Immunofluorescence Staining of Focal Adhesion

After 48 hours of incubation, some specimens were stained with fluorescence labeled antibodies to reveal proteins that were relevant to cytoskeleton and focal contact formation, i.e. actin and vinculin. The samples were removed from the multi-well plates before fixing the cells for 15 minutes in a 3.7% formaldehyde solution. All dilutions used in the staining procedure were made up in a buffer consisting of a 1:2000 dilution of 1M MgCl₂ in PBS (solution A). The cells on the sample surfaces were then permeabilized via exposure to a 0.5% Triton solution for 15 minutes. After the samples were rinsed in solution A, they were exposed to a primary antiserum, containing 1:300 dilution of the primary anti-vinculin antibody (Mouse anti-Vinculin, Sigma) in buffer solution plus 2.093 ovalbumin. The samples were incubated in the primary antiserum for 30 minutes in a humid, 37°C atmosphere. They were then thoroughly rinsed in buffer solution and incubated in a secondary antiserum, containing rhodamine phalloidin in 1:500 dilution, and a secondary antivinculin antibody (Goat anit-mouse, Molecular Probes) in 1:600 dilution in solution A plus 2.0% ovalbumin. The samples were incubated for 30 minutes at 37°C. A small drop of FluoroGuard reagent (Bio-Rad Laboratories, Hercules, CA) was added to the stained specimens before placing coverslips over the specimen. Immunofluorescence images were subsequently captured using optical microscopy.

3.2.3 Shear Assay Measurements

Samples for shear assay measurement were cultured for 48-hours incubation prior to the shear assay experiments. The cells were maintained, as described in the preceding section. The shear assay apparatus, shown in Figure 4.2, consists of a dual syringe Harvard pump (Harvard Apparatus, Holliston, MA), a heated water bath, an imaging system, and a Glycotech parallel plate flow chamber (Glycotech Corporation of Rockville, Maryland). During the shear assay experiment, fluid was pumped from one syringe of the Harvard Pump, through tygon tubing passing through

the water bath (to maintain fluid temperature at a biologically appropriate 37°C) and through to the parallel plate flow chamber. The parallel plate flow chamber, which has a diameter of **34 mm**, was placed inside the culture dishes. The flow channel consisted of a gasket attached via a vacuum seal to the flow chamber. The flow channel had a width of 2.5 mm and a height of 0.25 mm. Flow rates were set using a dual syringe pump, and increased at a rate of 50 mL/hour every minute. This was continued until all the cells within the viewing area were removed. Given the flow rate and volumetric limitations of the syringes compatible with our pump, it was necessary to use an appropriately viscous fluid for these experiments. Thus, a modified DMEM medium containing 3% (w/v) Methyl Cellulose Ethers (Sigma, St. Louis, MO) was used to increase the viscosity. At the same time, the large molecule cellulose greatly increased the non-Newtonian properties of the working solution. A rheometer (MCR501, Anton Parr, Ostfildern, Germany) was used to measure the viscosity of the working solution at different shear rates. The measured viscosities were incorporated into a computational fluid mechanics model of fluid flow in the shear assay chamber that is described in section 4.3. During the shear assay experiments, shearing was monitored with a Nikon Optiphot 66 reflected light microscope. The images were recorded digitally using a Sony 3CCD color video camera (Sony, Park Ridge, NJ) and a Pinnacle DV-Studio video capture device (Pinnacle, Mountain View, CA) with a resolution of 720 × 480 pixels. In all cases, the cell detachment conditions were established after 48-hour cell culture period. This allowed the trans-membrane and extra-cellular matrix proteins to be secreted and self-organized. The characteristic flow rate at detachment was determined by exposing 95 the cells to incrementally higher flow rates in the shear assay chamber, increasing the flow rate by 50 ml/h per minute by controlling syringe pump. At each time step, the number of detaching cells was counted. The characteristic flow rate at detachment was then taken to be the average of the detachment shear stress for all of the cells. For each material, 10 experiments were conducted, leading to data for approximately 150-200 cells per substrate. The measurements for

characteristic flow rate were combined with experiments done by former group members(Griffin, 2004,)

3.2.4 Staining of Cells for Cell Counting

Human ovarian carcinoma A2780 cells were then transferred from the surface and maintained in RPMI-1640 supplemented with 10% fetal bovine serum and 100 units/ml streptomycin and 0.4% trypan blue stain (Cat No. T13101). The Luna-II device was used on default protocol for all counts. The sample once resuspended was loaded into the proprietary loading bays and placed into the device for counting.

3.3 Protocol For Experimental Setup

Using a parallel flow plate chamber kit along with a double syringe pump allows for application of laminar flow to create shearing forces. Using the equation

$$\tau_w = \frac{6\mu Q}{wh^2} \quad (3.1)$$

where the shear force, τ_w , created by the laminar flow of the liquid over the surface can be calculated after the dynamic viscosity(μ) [assuming newtonian fluid], the flow rate Q, and the width (w) and height (h) are all known for the system. This allows a different shear stresses to be applied by varying the flow rate, at least in regular channel flow. In the case of the backward-facing step, the above relation cannot be used. Instead, equation 2.4 must be used with computational results in order to obtain the shear stresses near the walls of the backward facing step.

3.3.1 Protocol For Laminar Flow to Create Shear Forces

Materials

- Glycotech Parallel Flow plate Chamber Kit (figure above)
- Harvard Double Syringe Pump

- Tygon Tubing
- Teflon Tape
- Fluid (DMEM mixed with Sigma Methylcellulose for increased viscosity)

Procedure

1. Setup

1. Coat petri dishes/PDMS molds if applicable
2. Seed petri dishes cells for two days
3. Thoroughly clean all flow chamber parts and gasket before use and when switching petri dishes.
4. Mix DMEM with methylcellulose to create a viscous liquid that will not be harmful to the cells. (Create a 3% methylcellulose solution with DMEM from a 5% methylcellulose solution).
5. Begin warming the liquid in a hot water bath.
6. Wrap Teflon tape (included in the Glycotech parallel flow plate chamber kit) around each L-connector.
7. Insert the L-connectors into each flow bay (screw the connectors in by rotating the flow deck itself to avoid damaging the connectors)
8. Attach approximately three inches of silastic tubing to the L-connectors to serve as a junction to the Tygon tubing.
9. Connect lengths of 1/8 in. ID Tygon tubing to the input and output silastic tubing, the tubing connecting to the input bay should run through a hot water bath (37 degrees Celsius) to maintain good conditions for cell survival.
10. Connect a length of 1/8 in. ID tubing attached to a 3/8 in. ID tubing (parafilmmed to completely seal the attachment) and attach to a side arm flask connected to a vacuum.

11. Fill one 60cc syringe with the liquid.

2. Priming

1. Obtain cleaned flow deck and gasket from Glycotech kit.
2. Place a minimal amount of vacuum grease on the outer edge of the bottom of the deck.
3. Carefully place the gasket onto the deck lining up the indentations and ensuring a good seal forms. Make sure there are no air bubbles trapped in between the gasket and the deck.
4. Place the entire flow deck in a sterile petri dish for priming with the liquid.
5. Connect the 60cc syringe containing the liquid to the Harvard syringe pump – syringe 1. Connect that syringe to the input flow bay using the Tygon tubing.
6. Connect the empty 60cc syringe to syringe 2 on the Harvard syringe pump and to the output bay in the flow deck via the Tygon tubing.
7. Set the syringe pump to reciprocal mode (Pump one pushes out and Pump 2 draws in).
8. Prime the flow deck by filling it with the liquid running the pump at roughly 100 ml/hour.

3. Testing and Observation

1. Disconnect the tubing to the flow deck.
2. Remove the primed flow deck from the petri dish and replace the petri dish with a seeded petri dish.
3. Carefully lower the flow deck onto the seeded petri dish so as to minimize air bubbles and not to shear off any cells.
4. Use microscope and camera to image the cells through the flow path of the gasket.

5. Run the experiment at desired flow rates (ramping up to the desired flow rate at about an increase of 50ml/hr every 30 seconds). A flow rate of around 200ml/hr is adequate for HOSS cells incubated for 2 days on polystyrene.
6. Observe the behavior of the attached cells, note at what times and flow rates cells shear off, how many cells shear and at what rate. Increase the flow rate by 10ml/hr every minute once the cells begin to shear until cells are consistently shearing.

Protocol for Splitting/Passing Cells]

To grow cells in vitro, culture conditions must mimic in vivo conditions with respect to temperature, oxygen and CO₂ concentration, pH, osmolality, and nutrition. The main functions of the cell culture media are to maintain the pH and osmolality essential for cell viability and to provide the nutrients and energy needed for cell growth and multiplication. To do this we need:

- DMEM
- 2.5 % Trypsin
- (Phosphate- buffered Saline) PBS without Ca++ and Mg++

Procedure

1. 1. Warm working solution of Trypsin to 37 C.
 - Stock solution is 2.5% trypsin.
 - Dilute to 0.25% in PBS without Ca++ and Mg++ for working solution.
 - (i.e. 1 ml 2.5% Trypsin, 9 mls PBS w/o Ca++ and Mg++).
2. Remove media from flask by aspiration.
3. Add 2 mls trypsin to side of flask with cells on it. Remove by aspiration right away (removes surface proteins).

4. Add 2 mls trypsin to side of flask with cells on it, remove half of this promptly then incubate at 37 C for appropriate time to free cells (cap tightly closed while incubating). For HOS cells this is about 2-3 minutes (liberates cells from flask surface – breaks protein bonds attaching cells to surface).
5. Bang flask on counter to release cells.
6. Add 2-5 mls media to flask and remove all of contents to a 15 ml tube.
7. Spin down at 3.5k for 3 minutes.
8. Aspirate out supernatant leaving only pellet.
9. Re-suspend in 1ml media.
10. Use a portion of this to stock flasks (recommended 0.1 ml, or 0.2 mls).
Release cells into flask carefully.
11. Add an additional 10 mls media to the flask.
12. Place flask in incubator and loosen cap.

Cells are incubated in an incubator containing 5 % CO₂, 90 % humidity and held at a constant temperature of 37 C. When cells are growing at a low cell density or are in a lag phase, insufficient CO₂ may be produced to maintain the required optimal pH. For this reason the atmosphere of the incubator is maintained at around 5 % CO₂.

3.3.2 Protocol for Fixing Surfaces

When the cells reach the appropriate growth date they are removed from the medium and fixed in a glutaraldehyde solution to stop growth. Subsequently, the cells are put through a step-wise dehydration series and then critical point dried (final preservation step).

Reagents

- 25 % Glutaraldehyde solution (used to fix cells).

- 1 M phosphate buffer solution.
- Double distilled H₂O.

Procedure

1. Make 3% glutaraldehyde solution in 0.1 M phosphate buffer (glutaraldehyde is at 25% to start, make 1 M phosphate buffer and mix together, add sterile water to get end concentrations) Mix fresh for each time you use it, have at room temperature.
2. Remove cells from medium and rinse in 0.1 M phosphate buffer solution.
3. Put glutaraldehyde solution into well at appropriate amount to cover sample.
4. Place sample into this well with minimal disturbance.
5. Fix cells for 1 hr at room temperature and refrigerate overnight
6. Remove samples from glutaraldehyde solution and rinse in 0.1 M phosphate buffer solution.
7. Put samples through alcohol dehydration series (30%, 50%, 70%, 80%, 90%, 95%, 100% ethanol) with 30 minutes in each concentration at room temperature.
8. Critical point dry samples.

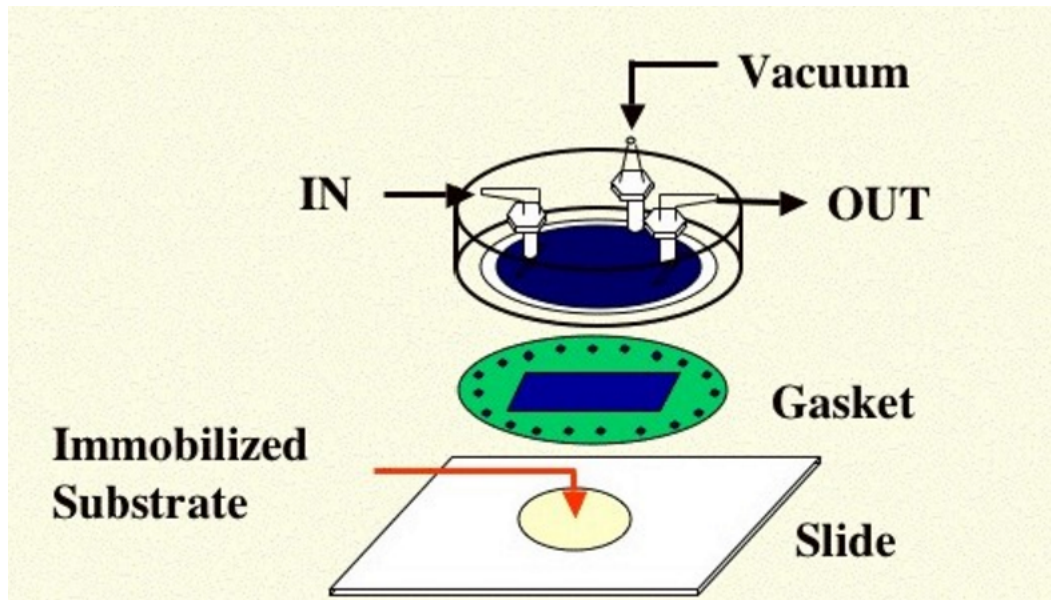


FIGURE 3.1: Schematic of Parallel Plate Flow Chamber.
Adopted from (Resto, V. A., 2008)

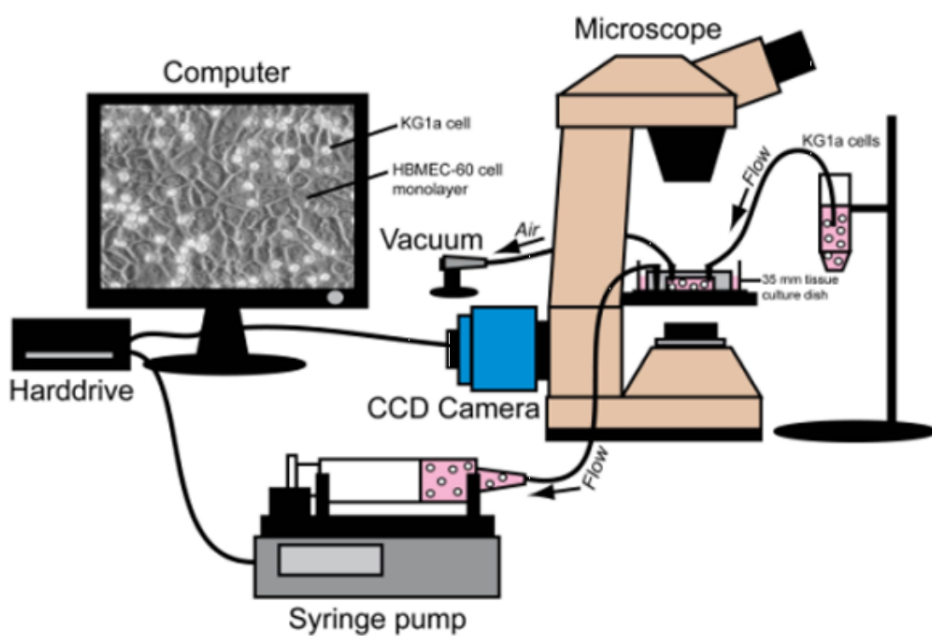


FIGURE 3.2: Shear Assay System Setup adopted from (Pins,
G. D, 2006)

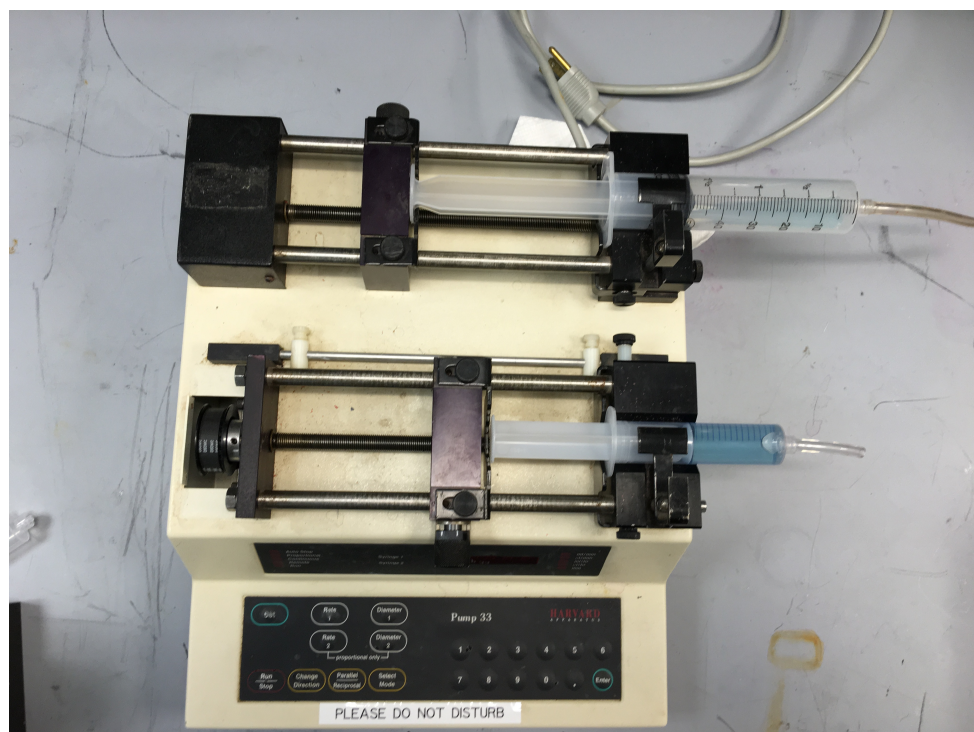


FIGURE 3.3: Harvard Apparatus Syringe Pump with 50 ml syringes

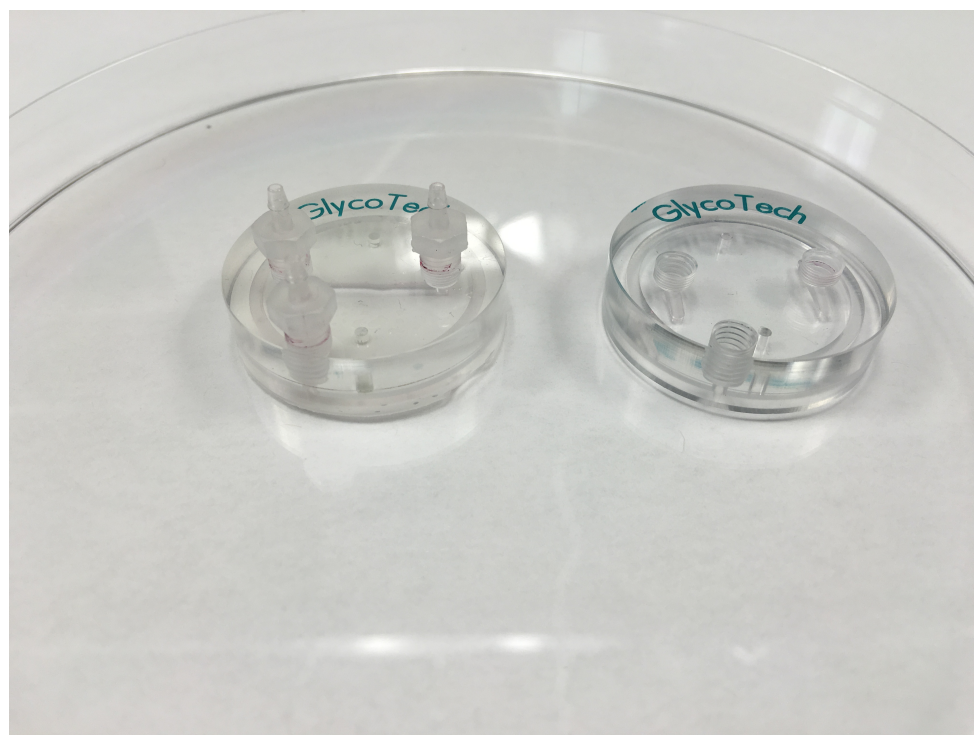


FIGURE 3.4: GlycoTech Parallel Plate Flow Chamber heads

Chapter 4

Computational Evaluation of Domain

4.1 Computational Model Of Experimental Setup

The computation model of the experimental setup chosen involved invoking solving the Navier-Stokes Equation in two dimensions over a backward facing step geometry by means of a finite difference method. This form was chosen to obtain an easily implemented solver for the Navier-Stokes that avoided the use of the Pressure-Poisson by using stream functions and vorticity to correct for velocities– rather than the primitive variable of P (by taking the curl of the equation). This made the implementation of the code much simpler since only two partial differential equations needed to be solved. This form of the Navier Stokes is also primary (mass) conservative and thus eliminates the question of meeting primary conservation that often plagues the computational fluid dynamicist.

The chosen finite difference operator was a centered-difference scheme. The centered difference scheme is second order accurate, which gives it an advantage over methods such as the backward or forward Euler schemes which are both first order in space. However, The upwind scheme (backward difference) is in general, more diffusive than the centered scheme. Furthermore, numerical analysis shows that it is more stable than centered schemes in space, which can lead to some spurious oscillations or dispersive errors. As a result, due to the possibility of oscillating behavior of the

centered scheme, especially in a convection dominated flow, the use of the upwind scheme could stabilize the solution.

Centered scheme:

$$\frac{\partial \omega}{\partial t} = A + B + C \quad (4.1)$$

Where A, B, C =

$$A = \frac{-1}{4\Delta x^2}((\psi_{i,j+1}^n - \psi_{i,j-1}^n)(\omega_{i+1,j}^n - \omega_{i-1,j}^n)) \quad (4.2)$$

$$B = (\psi_{i+1,j}^n - \psi_{i-1,j}^n)(\omega_{i,j+1}^n - \omega_{i,j-1}^n) \quad (4.3)$$

$$C = \frac{1}{Re} \left(\frac{\omega_{i+1,j}^n + \omega_{i-1,j}^n + \omega_{i,j+1}^n + \omega_{i,j-1}^n - 4\omega_{i,j}^n}{\Delta x^2} \right) \quad (4.4)$$

For the second derivative, a centered scheme is essential in order to prevent the rise of spurious oscillations in the velocity field of the result.

An explicit scheme was chosen for the temporal portion of the code due to its ease of implementation, scalability and lower computational cost when compared to other methods.

$$\omega_{i,j}^{n+1} = \omega_{i,j}^n + dt(A + B + C) \quad (4.5)$$

In order to have a solution that is convergent in space, we must impose a condition on the grid spacing as detailed below:

$$\frac{v\Delta t}{h^2} \leq \frac{1}{4} \quad (4.6)$$

$$\frac{(|u| + |v|)\Delta t}{v} \leq 2 \quad (4.7)$$

With the aforementioned restrictions and methods outlined, the pseudo code for the system can be written as:

1. Initial Vorticity given

2. Solve for the stream function
3. Find the vorticity and stream function at the boundary
4. find the RHS (A,B,C) of the vorticity equation
5. Update Interior vorticity
6. $t = t + \Delta t$
7. Use new vorticity to solve for part (2)

In order to achieve this, a certain set of numerical techniques and boundary conditions need to be explored. Firstly, consider the non-linear advection-diffusion equation in two dimensions. (We used this form because the pressure term is absorbed by the curl of the velocity field and the body force term is neglected) (Tannehill J, 2011):

$$\frac{\partial \omega}{\partial t} = -\frac{\partial \psi}{\partial y} \frac{\partial \omega}{\partial x} + \frac{\partial \psi}{\partial x} \frac{\partial \omega}{\partial y} + \frac{1}{Re} \left(\frac{\partial^2 \omega}{\partial x^2} + \frac{\partial^2 \omega}{\partial y^2} \right) \quad (4.8)$$

and the elliptic equation:

$$\frac{\partial^2 \psi}{\partial x^2} + \frac{\partial^2 \psi}{\partial y^2} = -\omega \quad (4.9)$$

require the following boundary conditions:

- Uniform inflow at the inlet. This was achieved using the following relation:

$$\frac{\partial \psi}{\partial y} = u \quad (4.10)$$

Therefore a constant gradient stream function, with gradient equal to the absolute value of u that would match the Reynolds Number, was prescribed at the inlet.

- No penetration of slip walls(zero tangential or normal velocities). To achieve this to second order, a three point stencil in the gradient of the stream function was used:

$$\psi_i = \frac{1}{4}\psi_{i+1} + \frac{3}{4}\psi_{i-1} \quad (4.11)$$

- Convective outflow at the outlet. This was achieved by setting the stream function and vorticity at the outlet to the value of each quantity, one point upstream.

$$\psi_i = \psi_{i-1} \quad (4.12)$$

$$\omega_i = \omega_{i-1} \quad (4.13)$$

The wall vorticity is found through a second-order central difference approximation using the stream function by the relationship (Tannehill J, 2011).

$$\omega_{\text{wall}} = \frac{\partial^2 \psi}{dx^2} \quad (4.14)$$

The elliptic equation [4.9] is solved using the numerical method known as Successive Over-relaxation (SOR). Through this method, the solution is iteratively *relaxed* to a steady-state in pseudo-time, α with a relaxation parameter β for stability (Tannehill J, 2011).

$$\psi_{i,j}^{\alpha+1} = \frac{\beta}{4}(\psi_{i,j}^\alpha + \psi_{i-1,j}^{\alpha+1} + \psi_{i,j+1}^\alpha + \psi_{i,j-1}^{\alpha+1} + h^2\omega_{i,j}^n) + (1 - \beta)\psi_{i,j}^\alpha \quad (4.15)$$

Visualization of these solutions was done through a plotting algorithm developed in MATLAB, detailed below.

4.2 Stability Analysis

The general heuristic stability of the non-linear advection diffusion equation in 2-D requires that the divergence of the velocity field be greater than

zero (Tannehill J, 2011). Hence:

$$\frac{c^2 \Delta t}{2} \leq \mu \quad (4.16)$$

or

$$\left(\frac{c \Delta t}{\Delta x} \right) \leq 2\mu \frac{\Delta t}{\Delta x^2} \quad (4.17)$$

which may be used to develop a very useful parameter when solving the Advection-Diffusion Equation on a uniform mesh: The "Mesh Reynolds Number" or Peclet Number, which is defined by:

$$\text{Re}_{\Delta x} = \frac{c \Delta x}{\mu} \quad (4.18)$$

This non-dimensional parameter characterizes the ratio between the convection and diffusion term and is very important if one wants to determine the character of the solution of the convection-diffusion equation(Tannehill J, 2011). Extending this result, and applying a more robust criteria for low Reynolds number flow using Fourier stability analysis, we obtain an amplification factor:

$$\left(\frac{c \Delta t}{\Delta x} \right)^2 \leq 2r \quad (4.19)$$

and

$$r \leq \frac{1}{2} \quad (4.20)$$

Finally this gives the stability criteria of:

$$2 \leq \text{Re}_{\Delta x} \leq \frac{2}{\frac{c \Delta x}{\Delta x}} \quad (4.21)$$

4.3 CFD Results

Below highlights selected plots of the results of the streamline vorticity solver for the backward facing step geometry for selected Reynolds Number. It is good to note at this point that the plotting functions in MATLAB, `quiver` automatically scales the length of arrows relative to each other. Though some arrows may seem much larger than others(particularly in the initial state), the ratio in the magnitude of their velocities with the mean velocity of the flow is at most 1.38.

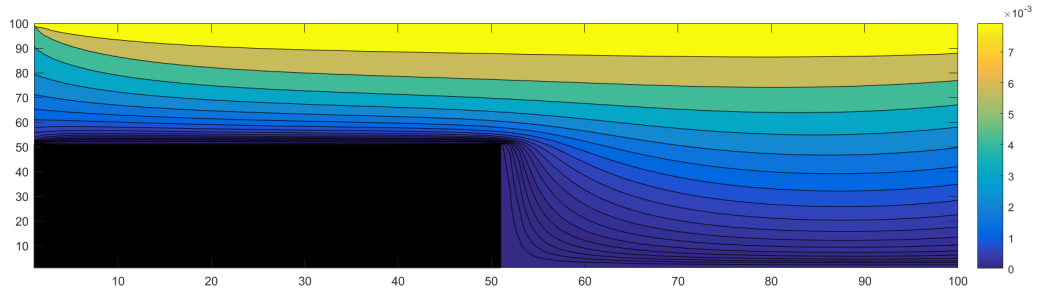


FIGURE 4.1: Contour Plot of Streamlines in a 100×100 grid domain for $\text{Re} = 0.1$. This plot shows the initial state of the system at time, $t = 0$

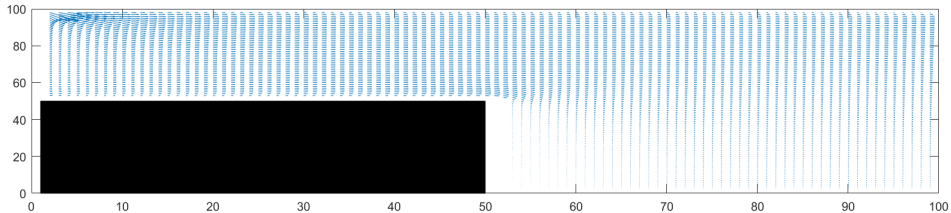


FIGURE 4.2: Quiver plot of velocities in a 100×100 grid domain for $\text{Re} = 0.1$. This plot shows the initial state of the system at time, $t = 0$

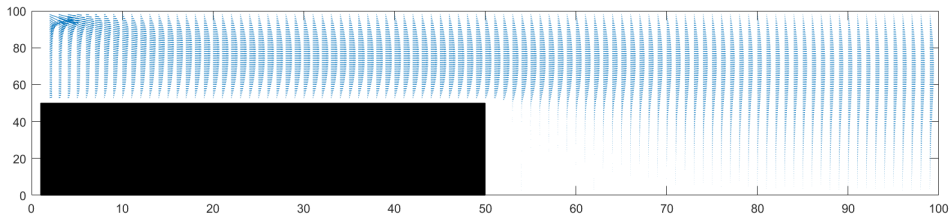


FIGURE 4.3: Contour Plot of Streamlines in a 100×100 grid domain for $\text{Re} = 0.3$. This plot shows the state of the system at long time

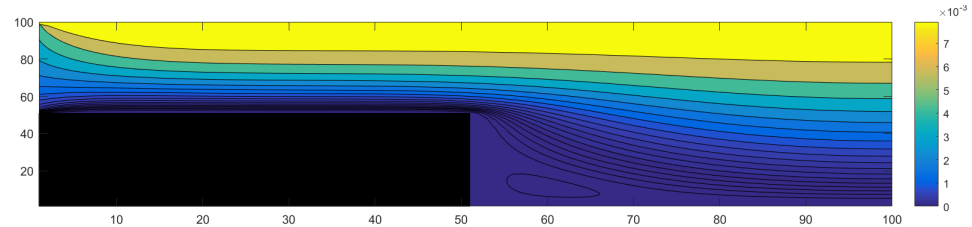


FIGURE 4.4: Quiver Plot of velocities in a 100×100 grid domain for $Re = 0.3$. This plot shows the state of the system at long time

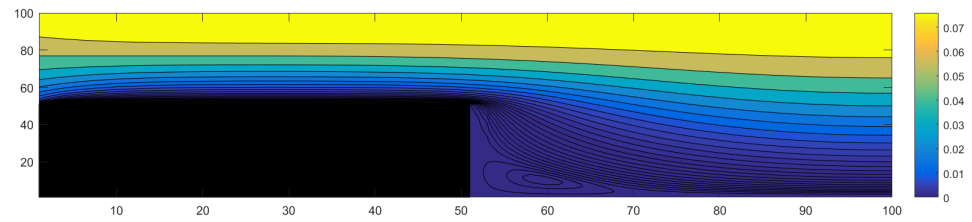


FIGURE 4.5: Contour Plot of Streamlines in a 100×100 grid domain for $Re = 0.6$. This plot shows the state of the system at long time

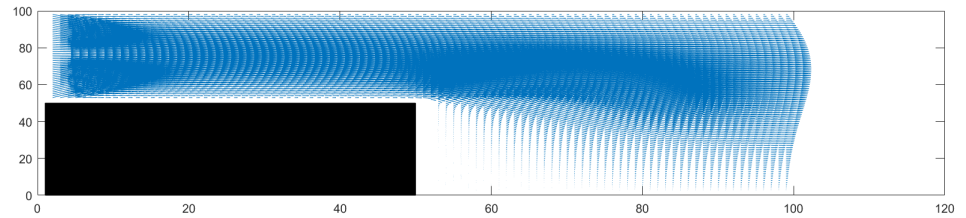


FIGURE 4.6: Quiver Plot of velocities in a 100×100 grid domain for $Re = 0.6$. This plot shows the state of the system at long time

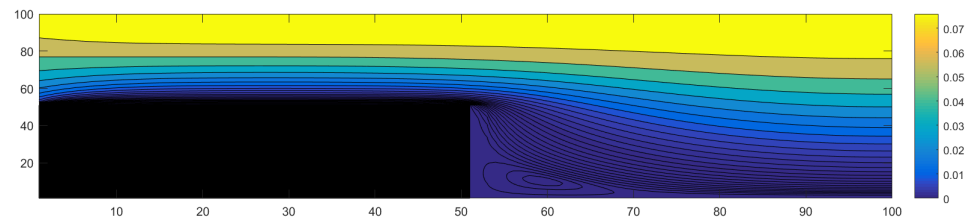


FIGURE 4.7: Quiver Plot of velocities in a 100×100 grid domain for $Re = 1$. This plot shows the state of the system at long time

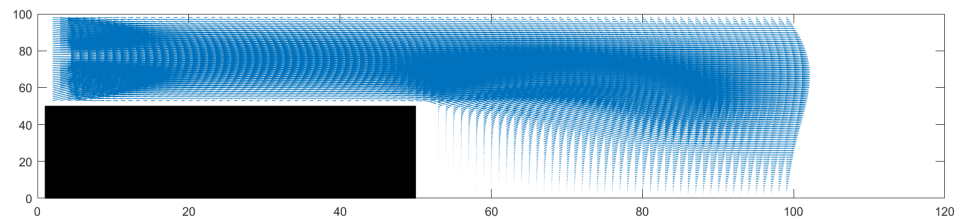


FIGURE 4.8: Quiver Plot of velocities in a 100×100 grid domain for $Re = 1$. This plot shows the state of the system at long time

4.3.1 MATLAB Code

```

1 % MAE 442- Thesis
2 % Backward Facing Data Plotter
3 % 2016
4 % Andre Douglas
5
6 % Description: Harvests the output from bfs.cpp and reorders the indices
7 % of the data sets of the relevant paramters and obtains contour and
8 % quiver plots
9 %%%%%%%%%%%%%%
10 clear all
11 close all
12
13 %Set up the format & size for plotting/movie
14 %Select what plots should be generated
15 plotquiver = true;
16 plotcontour = true;
17 %% load data sets from H drive
18 U = load('ufilebfs.txt');
19 V = load('vfilebfs.txt');
20 SF = load('sffilebfs.txt');
21 VT = load('vtbfs.txt');
22 MESH = load('meshbfs.txt');
23
24 %% Sets Dimensions of New Arrays
25 xdim = size(U,1);
26 ydim = size(U,2);
27 u = zeros(xdim, ydim);
28 v = zeros(xdim, ydim);
29 sf = zeros(xdim, ydim);
30 vt = zeros(xdim, ydim);
31 for i = 1:1: ydim
32     for j = 1 : 1 : xdim
33         u(j,i) = U(xdim+1 - j, i);
34         v(j,i) = V(xdim+1 - j, i);
35         sf(j,i) = SF(xdim+1 - j, i);
36         vt(j,i) = VT(xdim+1 - j, i);

```

```
37         mesh(j,i) = MESH(xdim+1 - j, i);
38     end
39 end
40
41 max(-U(:)) %Outputs maximum U velocity in domain (a check for convergence)
42
43 %% Generates plots
44 if(plotquiver == true)
45     figure(1)
46
47     n = 1;
48     scale = 4; %Length of arrows
49     set(gcf, 'Position', [50 150 1300 250]); %Fixes Window Geometry
50     ur = -u(1:n:size(u,1),1:n:size(u,2));
51     vr = v(1:n:size(u,1),1:n:size(u,2));
52     quiver(ur,vr, scale);
53     hold on;
54     A = ones(1,floor(50/n))*floor(50/n); %Generates BFS
55     q = area(A);
56     set(q(1), 'FaceColor', [0,0,0]);
57     hold off;
58 end
59 if(plotcontour == true)
60
61     figure(2)
62     set(gcf, 'Position', [50 150 1300 250])
63     contourf(sf,logspace(-7,0,51)-0.000025);
64     colorbar
65     hold on
66     rectangle('Position',[1 1 50 50], 'FaceColor', [0; 0; 0]);
67     hold off;
68 end
```

4.3.2 C++ Code

```

1 #include <stdio.h>
2 #include <math.h>
3 #include <iostream>
4 #include <Eigen/Core>
5 #include <Eigen/LU>
6 #include <fstream>
7 #include <assert.h>
8
9 #define T_def 0.01
10 #define N_def_x 100
11 #define N_def_y 100
12
13 using namespace std;
14 using Eigen :: MatrixXd;
15 using Eigen :: VectorXd;
16
17 MatrixXd sor(int N, int M, double beta, double hx, double hy,
18               MatrixXd vt, MatrixXd sf, MatrixXd W, MatrixXd mesh, int
19               maxstep, int maxit, double maxerr, int scalex, int scaley)
20 {
21
22     int k;
23     int l;
24
25     for (k = 0; k < maxstep; k++)
26     {
27         for (l = 0; l < maxit; l++)
28         {
29             W = sf;
30             for (int i = 1; i < N-1; i++)
31             {
32                 for (int j = 1; j < M-1; j++)
33                 {
34                     if (mesh(i, j) == 0)
35                     {
36                         if (mesh(i+1, j) == 0)
37                         {
38                             if (mesh(i-1, j) == 0)
39                             {
40                                 if (mesh(i, j+1) == 0)
41                                 {
42                                     if (mesh(i, j-1) == 0)
43                                     {
44                                         if (mesh(i+1, j+1) == 0)
45                                         {
46                                             if (mesh(i+1, j-1) == 0)
47                                             {
48                                                 if (mesh(i-1, j+1) == 0)
49                                                 {
50                                                     if (mesh(i-1, j-1) == 0)
51                                                     {
52                                                         if (beta * (vt(i, j) + (W(i, j) / 8) * (vt(i+1, j) + vt(i-1, j) + vt(i, j+1) + vt(i, j-1) + vt(i+1, j+1) + vt(i+1, j-1) + vt(i-1, j+1) + vt(i-1, j-1))) >= T_def)
53                                                         {
54                                                             vt(i, j) = beta * (vt(i, j) + (W(i, j) / 8) * (vt(i+1, j) + vt(i-1, j) + vt(i, j+1) + vt(i, j-1) + vt(i+1, j+1) + vt(i+1, j-1) + vt(i-1, j+1) + vt(i-1, j-1)));
55                                                         }
56                                                     }
57                                                 }
58                                             }
59                                         }
60                                     }
61                                 }
62                             }
63                         }
64                     }
65                 }
66             }
67         }
68     }
69 }
```

```

34 sf(i,j) = 0.25*beta*(sf(i+1,j)+sf(i-1,j)+sf(i,j+1)+sf(i,j-1) +
35   hx*hy*vt(i,j))+(1.0-beta)*sf(i,j);
36 }
37 }
38 double Err = 0.0;
39 for(int i = 0; i < N; i++)
40 {
41 for(int j = 0; j < M; j++)
42 {
43 Err = Err + abs(W(i,j)-sf(i,j));
44 }
45 }
46
47 // cout << Err << endl;
48 if(Err <= maxerr)
49 {
50 return sf;
51 break;
52 }
53 }
54 }
55 }
56 assert(0); //convergence not reached
57 }

58

59 MatrixXd upvort (int N, int M, double hx, double hy, MatrixXd W
60   , double t, MatrixXd sf, MatrixXd vt, int scalex, int scaley
61   , double U, double C)
62 {
63
64
65 //solve for the vorticity at the walls
66 //top wall
67 for (j = 1; j < M-1 ; j++)
68 {
69 vt(1,j) = 2.0*(sf(1,j) - sf(2,j))/(hy*hy);

```

```

70 }
71 //top of step wall
72
73 for(j = 1; j <= scalex; j)
74 {
75   vt(scaley-2, j) = 2.0*(sf(scaley-2, j) - sf(scaley-3, j)) / (hy*hy
    );
76 }
77
78 //side of step wall
79
80 for( i = scaley-1; i < N-1; i)
81 {
82   vt(i,scalex+1) = 2.0 * (sf(i, scalex+1)- sf(i, scalex+2)) / (hy*
     hy);
83 }
84
85 // cout << vt << endl
86 //bottom wall right of step wall
87
88 for(j = scalex; j < M-1; j)
89 {
90
91   vt(N-2, j) = 2.0 * (sf(N-2, j) - sf(N-3, j)) / (hy*hy);
92 }
93
94 //for ( i = scaley; i < N-1; i)
95 //{
96 //  for ( j = 0; j < scalex; j)
97 //  {
98 //    vt(i,j) = 0; // enforce vorticity condition
99 //  }
100 //}
101 //cout << sf << endl;
102 return vt;
103
104 }
105

```

```

106 MatrixXd wsolve (MatrixXd sf, MatrixXd vt, double Re, double hx
107   , double hy, int N,int M, MatrixXd W, MatrixXd mesh)
108 {
109
110   int i;
111
112   for(i = 1; i < N-1; i++)
113   {
114     for(j = 1; j < M-1; j++)
115     {
116       if(mesh(i,j) == 0)
117       {
118         W(i,j) = -0.25*((sf(i,j+1) - sf(i,j-1)*(vt(i+1,j) - vt(i-1,j))-
119           sf(i+1,j) - sf(i-1,j))*(vt(i,j+1) - vt(i,j-1)))/(hx*hy) +
120           1/Re * (vt(i+1,j) + vt(i-1, j) + vt(i,j+1) + vt(i, j-1) -
121           4.0* vt(i,j))/(hx*hy);
122     }
123   }
124
125   double ufunc(MatrixXd sf, double hx, double hy, int i, int j,
126                 MatrixXd u, MatrixXd mesh)
127   {
128     if(mesh(i,j) == 0)
129     {
130       u(i,j) = 0.5/hx * (sf(i+1, j) - sf(i-1, j));
131     }
132   }
133
134   double vfunc(MatrixXd sf, double hx, double hy, int i, int j,
135                 MatrixXd v, MatrixXd mesh)
136   {
137     if (mesh(i,j) == 0)
138     {

```

```

139 v(i,j) = -0.5/hy *(sf(i, j+1)-sf(i, j-1));
140 }
141 else {
142 v(i,j) = 0;
143 }
144 return v(i,j);
145 }
146
147 MatrixXd setgeo(int scalex, int scaley, MatrixXd mesh, int M,
148 int N)
149 {
150 int i;
151 int j;
152 for (j = 0; j <= scalex+1; j++)
153 {
154 for(i = scaley-2; i < N-1; i++)
155 {
156 mesh(i, j) = 1;//set mesh geometry to one all over bfs
157 }
158 }
159
160 for (j = 0; j < M; j++)
161 {
162 mesh(N-2, j) = 1;
163 mesh(N-1, j) = 1;//bottom streamline equal to box
164 }
165
166 for (j = 0; j < M; j++)
167 {
168 mesh(1, j) = 1;
169 mesh(0, j) = 1; //top mesh component
170 }
171
172 mesh(scaley-2, scalex+1) = 0;
173 //mesh(N-2, scalex+1) = 0;
174 return mesh;
175 }
176

```

```
177 //solve for the vorticity equation
178 int main()
179
180 {
181
182     int i;
183     int j;
184     int M = N_def_y;
185     int N = N_def_x;
186     double Re = 10;
187     double t = 0;
188     double T_max = T_def;
189     int maxit = 500;
190     int maxstep = 70;
191     double maxerr = 0.001;
192     double beta = 1.7;
193     double hx = 1.0/(N-1);
194     double hy = 1.0/(M-1);
195     int scalex = 50;
196     int scaley = 49;
197     scaley = N-scaley-1; //N - amount
198 //scaley = 0;
199     double pref = 0.25;
200     double U = 1.0;
201     double C = scaley;
202     double visc = 1/Re;
203     double dt = (hx*hy)/(4.0*visc);
204     cout << "Tstep : " << dt << endl;
205     cout << "Num. Time Steps : " << T_def/dt << endl;
206     MatrixXd sf (N,M);
207
208
209     MatrixXd vt (N,M);
210     MatrixXd W (N,M);
211     MatrixXd u (N,M);
212     MatrixXd v (N,M);
213     MatrixXd mesh (N,M);
214
215 //initialize the arrays to zero
```

```

216 for (i = 0; i < N; i++)
217 {
218     for(j =0; j < M; j++)
219     {
220         sf(i,j) = 0;
221         vt(i,j) = 0;
222         W(i,j) = 0;
223         u(i,j) = 0;
224         v(i,j) = 0;
225     }
226 }
227 //Calculate Peclet, Courant, Diffusion Numbers
228
229
230 double Co = U*dt/hx;
231 double D = (visc*dt) / (hx*hx);
232 double Pe = Co/D;
233 cout << "Co Number :" << Co << endl;
234 cout << "Diff. Number :" << D << endl;
235 cout << "Pe Number : " << Pe << endl;
236
237 if (Pe <= 2.0/Co && Pe >= 2*Co)
238 {
239
240
241 //Obtain the mesh that will be used to reference everything
242 mesh = setgeo(scalex, scaley, mesh, M,N);
243
244
245
246 //cout << mesh << endl;
247 for (t = 0; t < T_max; t+=dt)
248 {
249     //sf side wall
250     for ( i = scaley-2; i <= N-2; i++)
251     {
252         sf(i, scalex+1) = pref * sf(i, scalex+2);
253     }
254 //top wall stream function requirement

```

```

255 for (j = 0; j < M-1; j++)
256 {
257   sf(0,j) = U*hx*10.0;
258   sf(1,j) = 0.25 * sf(2,j)+ 0.75*sf(0,j);
259 }
260
261 //initialize stream fnc initial condition at left-most wall
262 for(i = 2; i < scaley-2; i++)
263 {
264   sf(i,0) = U*hx*10.0/((N-1)/2.0) * (scaley-i); //i/(N-1);
265   vt(i,0) = 0;
266 }
267 //sf requirement top of step
268 for(j = 0; j <= scalex; j++)
269 {
270   sf(scaley-2, j) = pref * sf(scaley-3,j); //sf(scaley-3 , j);
271 }
272
273 //sf bottom wall
274 for(j = scalex+1; j < M-1; j++)
275 {
276   sf(N-2, j) = pref * sf(N-3, j);
277 }
278
279
280 //Solve for the streamfunction by SOR methiod
281 sf = sor(N, M, beta, hx, hy, vt, sf, W, mesh, maxstep, maxit,
282           maxerr,scalex, scaley);
283
284 //Solve for vorticity at each boundary (UGH! !????)
285 vt = upvort(N,M,hx,hy, W, t, sf, vt, scalex, scaley, U,C);
286
287 //Solve for the rhs of the vorticity equation
288 W = wsolve(sf, vt, Re, hx, hy, N,M, W, mesh);
289
290 //update vorticity at time step
291 for( i = 1; i < N-1; i++)
292 {

```

```

293 for ( j = 1; j < M-1; j++)
294 {
295 vt(i,j) = vt(i,j) + dt*w(i,j);
296 }
297 }
298
299 //zero velocity gradeint at outflow
300
301 for ( i = 0; i < N ; i++)
302 {
303 //actually 2nd derivative of stream function
304
305 sf(i, M-1) = sf(i, M-2);
306 vt(i, M-1) = vt(i, M-2);
307
308 }
309 cout << "time : " << t << endl;
310
311 } // steady state velocity
312 //Obtain velocity arrays
313 for (i = 1; i < N-1; i++)
314 {
315 for (j =1; j < M-1; j++)
316 {
317 u(i,j) = ufunc(sf, hx, hy, i, j, u, mesh);
318 }
319 }
320 for (i = 1; i < N-1; i++)
321 {
322 for ( j = 1; j < M-1; j++)
323 {
324
325 v(i,j) = vfunc(sf, hx, hy, i, j, v, mesh);
326 }
327
328 }
329 }
330
331 //Write to datafiles for matlab to process

```

```
332    ofstream myfile;
333    myfile.open ("sffilebfs.txt");
334    myfile << sf;
335    myfile.close ();
336    //cout << u << endl;
337    ofstream myfile2;
338    myfile2.open ("vfilebfs.txt");
339    myfile2 << v;
340    myfile2.close ();
341    //cout << v << endl;
342    ofstream myfile3;
343    myfile3.open ("ufilebfs.txt");
344    myfile3 << u;
345    myfile3.close ();
346
347    ofstream myfile4;
348    myfile4.open ("meshbfs.txt");
349    myfile4 << mesh;
350    myfile4.close ();
351
352    ofstream myfile5;
353    myfile5.open ("vtbfs.txt");
354    myfile5 << vt;
355    myfile5.close ();
356 }
357 else {
358 cout << "Conversion Criteria Not Met" << endl;
359 }
360
361 return 0;
362 }
```

4.4 Validation of Results with Commercial Code

In order to validate the aforementioned backward facing step code, the same initial and boundary conditions were used to define a simulation in a commercial code: Autodesk Inventor CFD. The velocity fields and the shear rates at the wall were compared to see how accurate the methods coded were. Autodesk CFD uses a finite element/finite volume solver in order to solve the domain.

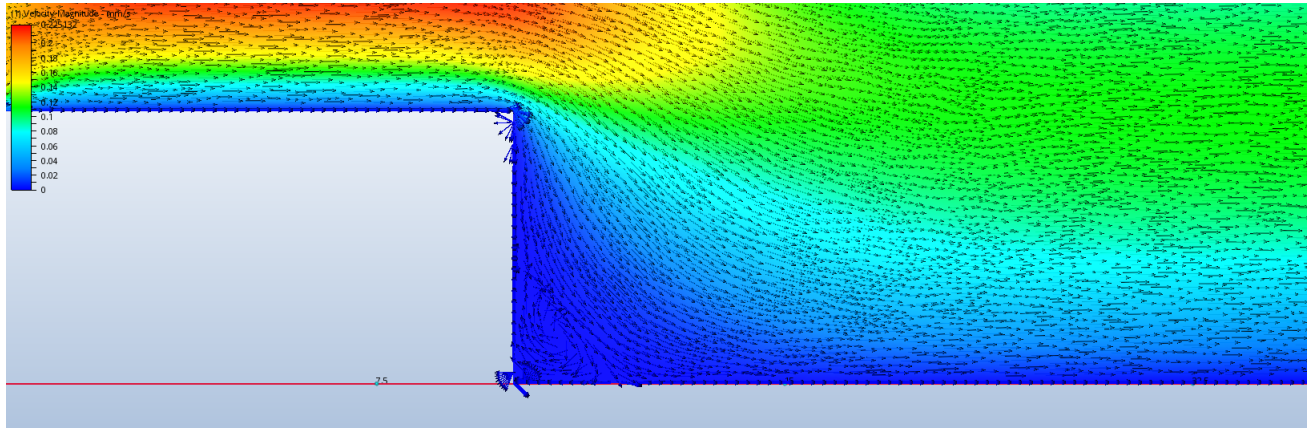


FIGURE 4.9: Recirculation zone from FEM simulation on AutoDesk CFD Suite for Reynolds Number 0.3. Note the Similarity between this figure and figure 4.5.

Validation was done by assuming the Autodesk solution to be more accurate., The C++ Finite Difference simulation is then compared to the Autodesk solution in terms of the mean flow velocity, vortex reattachment length, maximum and minimum velocity in the domain. These are tabulated below for Reynolds Number 0.3:

TABLE 4.1: Validation Parameters

Parameter	Autodesk Value	bfs.cpp Value	% Difference
Mean Velocity (U)	0.427	0.391	8.4
Mean Velocity (V)	0.101	0.0948	6.14
Vortex Reattachment Length	0.443b	0.429b	3.26
Max Velocity (U)	1.20	1.23	2.43
Min Velocity (U)	0	0	0
Max Velocity (V)	0.846	0.871	2.96
Min Velocity (V)	0	0	0

Noting the small differences in the validation values, it is safe to say that

the written computation code matches the commercial computation result well. For the remainder of the discussion, bfs.cpp will be used as its computational time was significantly less than Autodesk inventor.

Chapter 5

Experimental Results and Discussion

Preliminary results on the shear assay channel were promising. In order to get a better understanding of the parameters that govern the physiological flow, a first order estimate characterizing the system was done. Using flow data: the average Shear Rate and Shear Stress in various blood vessels, the Reynolds numbers were calculated.

These calculated Reynolds Numbers were also crossed referenced with a tabulated series of Reynolds numbers (Re^3) for the same blood vessels(Theodoros, 2005).¹ Together this gave the experiment a psychological range of Re to work with.

TABLE 5.1: Flow Parameters of Various Blood Vessels

Blood Vessel	Shear Rate (s^{-1})	Shear Stress(dyn/cm ³)	Diameter(μm)	Re^2	Re^3
Arterioles	1600	53	37	0.78	0.70
Capillaries	1300	42	9.0	0.0037	0.002
Venules	350	16	20	0.069	0.01
Arteries	270	11	15000	415	500

Using these Re as a guideline and only considering the small Reynolds Number range [$Re \ll 1$], the number of cells that remained at each Reynolds number increment was counted using image processing from stained cells obtained by a Luna II Automated Cell Counter. Interesting, a figure 5.1 will detail, in the limit of small Re , there seems to exist a critical Re , Re_c , above which, cell adhesion becomes increasingly difficult.

¹<http://www.coheadquarters.com/PennLibr/MyPhysiology/lect5/table5.01.htm>

5.1 Shear Assay Adhesion Results

5.1.1 Straight Channel Case

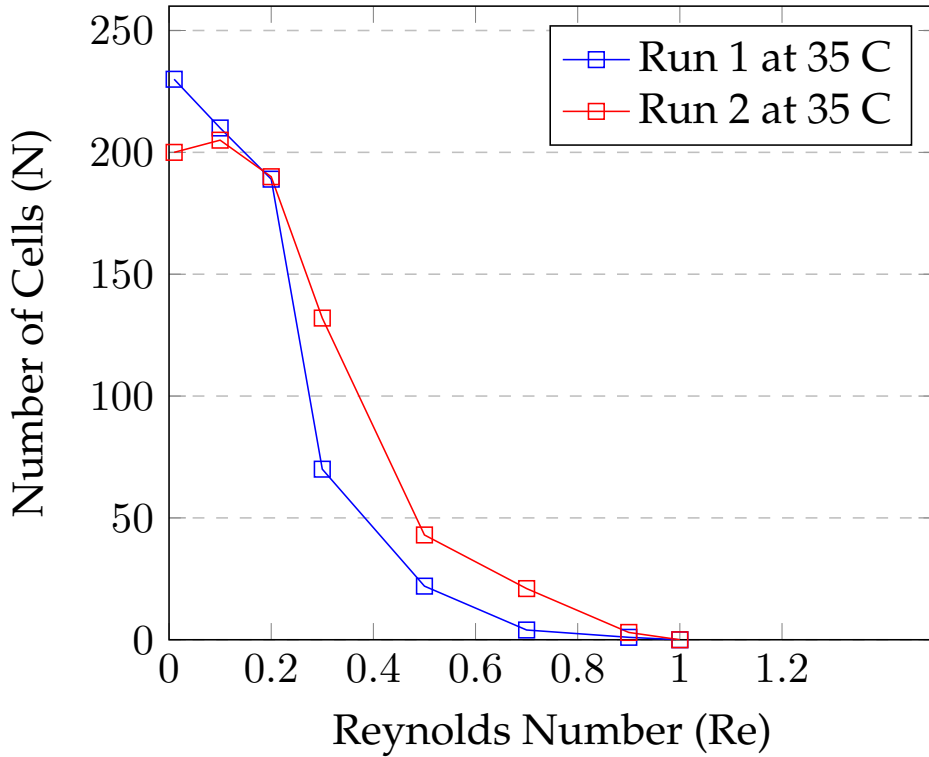


FIGURE 5.1: Reynolds Number Dependence on No. Adhering Cells PDMS Channel - Straight

In Figure 5.1, the Reynolds Number was varied from 0.001 to 1 by changing the flow rate in the experimental setup appropriately. Interestingly, at $Re = 0.1 - 0.3$, a large change in the number of cells adhered to the wall occurred. It is possible that within this range of Reynolds Numbers, the critical Reynolds number may exist for the straight channel. Examining the Reynolds Number range specified above using the Shear Assay Device, yielded the results shown in figure 5.2 below. The existence of a critical Reynolds is not clear when the range of Reynolds prescribed range of Reynolds numbers is examined. Until Reynolds Number 0.15 the number of cells is fairly constant until about Reynolds Number 0.20 where a sharp decline in the number of cells is observed. This rapid decline becomes more and more amplified as the Reynolds Number is increased past 0.2. For the cases where initial number of cells (N) was 250, the ratio to the number of

cells at the expected RC_c and the initial number of cells is about 0.71 while for the run with a larger initial mass of cells, the same ratio is about 0.53.

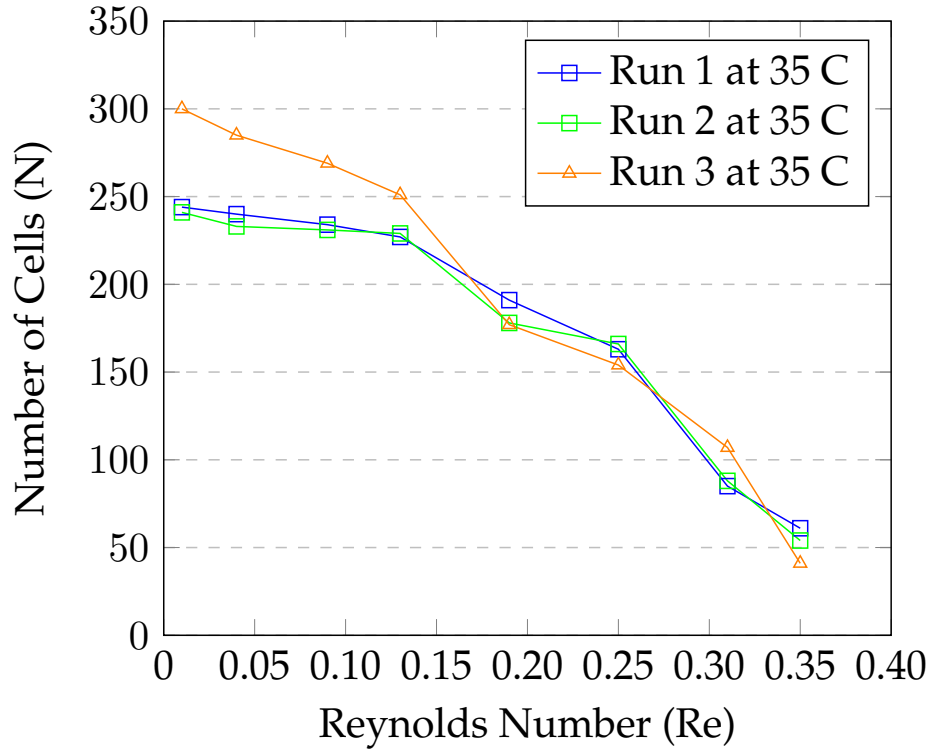


FIGURE 5.2: Reynolds Number Dependence on No. Adhering Cells PDMS Channel - Straight

Seeing the ambiguity in the dimensional data plots, non-dimensionalization of the data could be used to verify the hypothesis in a more rigorous manner. Consider the parameters of the system:

- u - velocity
- μ - viscosity
- H - height of the channel
- b - cell height
- τ_c - critical shear stress
- γ_c - critical shear rate of the cell
- N - number of cells

Using Buckingham Pi Theorem, two sets of three non-dimensional groups could be derived:

$$\frac{N}{N_0} = f \left(\frac{b}{H}, \frac{\tau H}{U\mu}, \frac{\tau_c H}{U\mu} \right) \quad (5.1)$$

$$\frac{N}{N_0} = f \left(\frac{b}{H}, \frac{\tau H}{U\mu}, \frac{\gamma_c H}{U} \right) \quad (5.2)$$

The nondimensional numbers: the nondimensional shear stress: $\tau* = \frac{\tau_c H}{U\mu}$ and the nondimensional shear rate: $\gamma* = \frac{\gamma_c H}{U}$ are of particular interest because they will aid the experiment on determining if a relationship between the adhesion of cancer cells and shear stress or shear rate. For the remainder of this chapter, $\frac{N}{N_0} = \eta$. In order to test the relationship, a second parameter: the viscosity of the fluid, needed to be varied. In order to do this, water was mixed with a non-ionic solute called hydroxyethylcellulose – commercially known as Natrosol. Using a calibration curve provided by the manufacturers, the viscosity of solutions of known weight percentages could be determined. The results are shown in the table below:

TABLE 5.2: Natrosol viscosities by weight percentage in water at 35 C

Viscosity (mPa s)	Weight Percentage
0.692	0
1.00	0.23
1.60	0.38
5.00	0.64
9.20	1.10
13.8	1.81

Running these shear assay device with these various fluids at these viscosities with increasing velocity garnered the results seen in figures 5.2 and 5.3 below.

The most interesting take away from the aforementioned figures is the differences in the dimensional and non-dimensional plots. In figure 5.3, the cell ratio, that is the number of cells normalized by the initial number of cells, is plotted against the shear stress experienced by the cell in Poiseuille

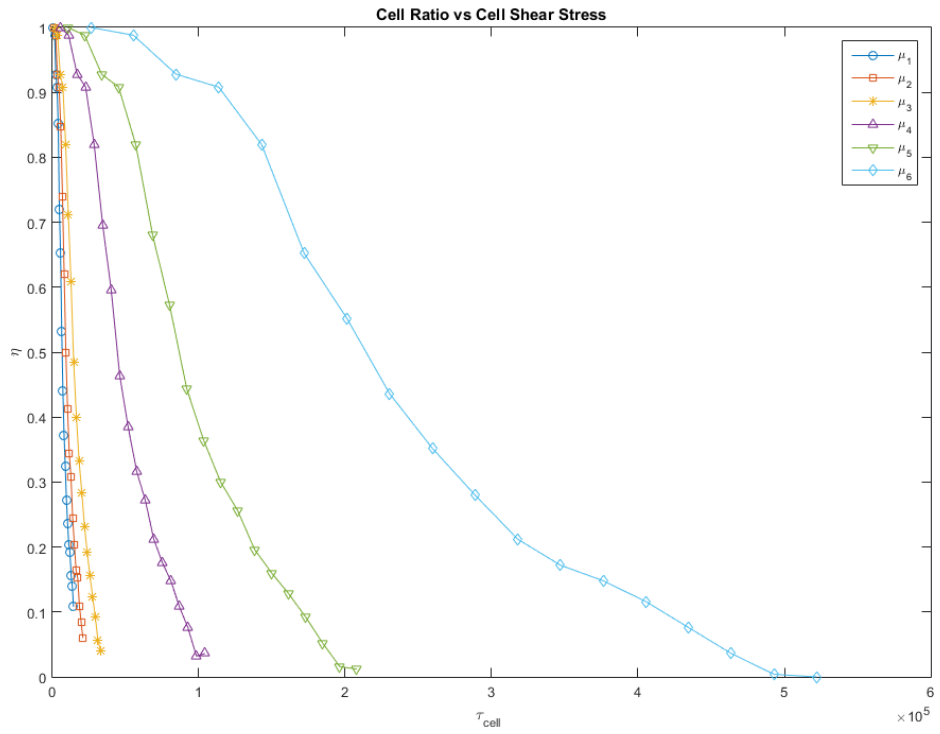


FIGURE 5.3: Plot of the Cell Ratio η vs. shear stress γ^* for different viscosities, μ

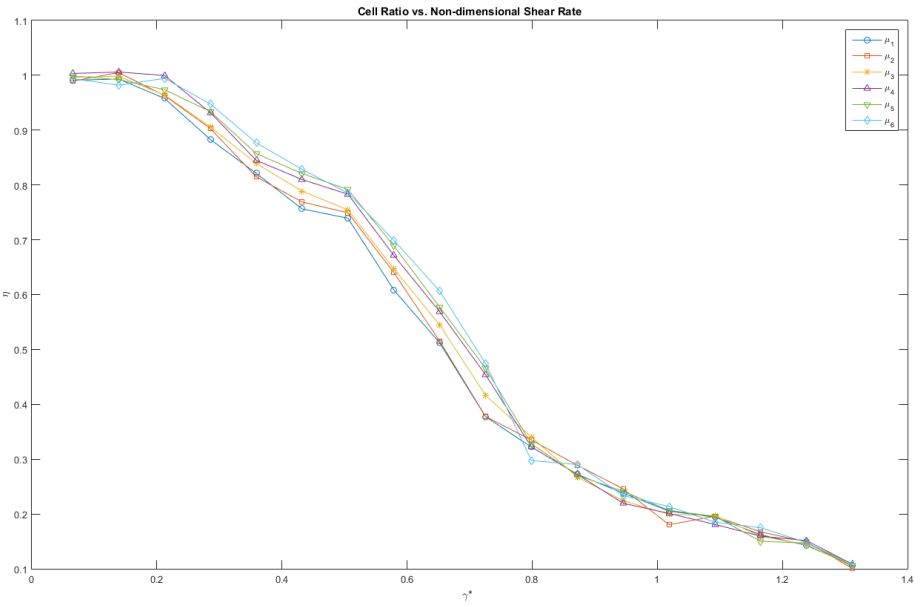


FIGURE 5.4: Plot of the Cell Ratio η vs. non-dimensional shear rate γ^* for different viscosities, μ

flow. Unexpectedly, in this low Reynolds Number regime, figure 5.3 suggests that there is not a strong relationship between shear stress and cell

adhesion. As the viscosity of the fluid is increased from the lowest, μ_1 to highest, μ_6 , the ease of removal decreases markedly. The critical shear stress is obtained from (Fu, 2019). This increase gives an clue about the physics of the system by showing that there may exist a viscosity independence. That is, at some shear rate γ_c required to get some τ_c required for detachment is changing and τ_c is not dependent on viscosity.

This case is further illuminated through figure 5.3. This plot of Cell Ratio against non-dimensional Shear Rate, defined in this case as $\frac{U}{\gamma_c H}$, where U is the velocity, γ_c is the critical shear stress as defined in Ruoslahti, 1996 and H is the channel height. This plot is demonstrates a strong relationship between cell adhesion and shear rate particularly at higher velocities. This dependence on shear rate also shows viscosity independence through the following observation: higher viscosities result in lower shear rates for a given τ_c and thus higher cell retention. This data obtained by averaging over many trials, shows that cell adhesion may be a strong function of the shear rate.

To further understand what this data means, let us examine biologically and fluid mechanically, why this result may be valid. Shear rate is defined as the velocity gradient in a fluid. Consider now cells adhered to the surface of PDMS. As discussed in chapter 1, cells form connections with the surface of whatever medium they are adhering to, by and intermediate protein layer called the ECM. The ECM facilitates bonds to the cells by way of strong electrostatic interactions called hydrogen bonds. To remove adhered cells, a tug-of-war between two kinetic process must take place in the cell-wall contact area: bond formation and rupture. In order to rupture the hydrogen bond, the distance between the interacting protein structures must be increased or energy must be applied to the bond, sufficient to result in bond breaking. Since the latter isn't the case in this system, it makes more sense to consider the former.

How can shear rate contribute the extension of hydrogen bonds, resulting

in eventual bond breaking? Well consider the tension in a bond that is subjected to a force on it. If we integrate over all the bonds in the cell-wall interface, we arrive at a total tension, T_{tot} . Using the arguments posed by Hammer DA, 1989, this total tension can be related to the loads and the torques due to those loads by mechanical equilibrium equations. These torques are what stretch the bonds and – which may lead to bond breaking and result in adhesion failure at the walls and it is directly related to the shear rate at the walls. But does that mean that shear stress does not play any role in any of this? It is difficult to say as a wide region of non-dimensional shear rate does not agree perfectly with the assumption that cell adhesion is only a function of shear rate. It is likely that both forces play an important roll in cell adhesion but for higher velocities, it is the shear rate that matters the most.

To further explore the possible relationship between τ and γ_c , we may consider arguments in Material Science. The response of living tissue to loading may be described physically using constitutive models of linear viscoelasticity (Biswas, 2015). With this model, the stress-strain or force-displacement interactions can be approximated using a linear combination of springs and dashpots.

For viscoelastic materials, the relationship between stress and strain can be expressed generally as:

$$\sigma = \sigma(\epsilon, \dot{\epsilon}) \quad (5.3)$$

Equation 5.3 agrees states that stress(σ) is not only a function of strain(ϵ) but also strain rate($\dot{\epsilon}$) and that the stress-strain diagram of a viscoelastic material is not unique but is dependent upon the rate at which the strain is developed on the material (Ozkaya, 2012).

We can use this analogy to make observations about the results seen in figure 5.4. We know that there exists a critical shear stress above which most cells will become sheared off. With increasing shear rate, which is analogous with strain rate (Ozkaya, 2012), we see from figure 5.5 that we achieve

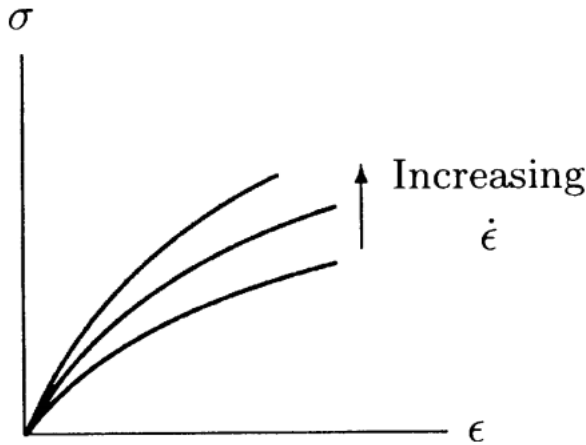


FIGURE 5.5: Strain rate ($\dot{\epsilon}$) dependent viscoelastic behavior.
Adopted from (Ozkaya, 2012)

higher stress values in a shorter time. In other words, higher shear rates result in the critical shear stress (τ_c) being achieved quicker. As a result, shear stress may not be the strongest parameter in the system of cell adhesion since even though there exists some shear stress (τ_c) above which the majority of cells detach, it is the shear rate that determines how quickly that shear stress is achieved. By considering the viscoelasticity of the cell we can

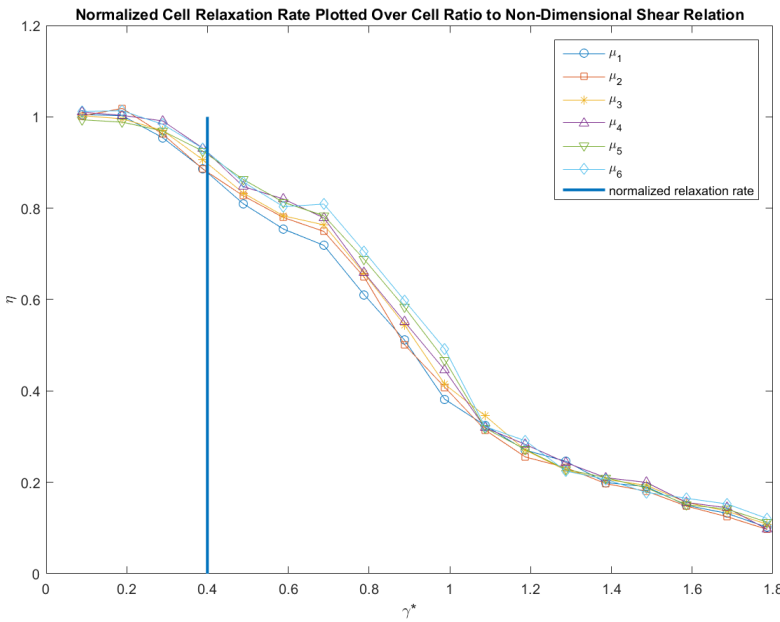


FIGURE 5.6: Inclusion of Relaxation Time in Shear Rate Plot

define the cell's relaxation rate(λ) as:

$$\lambda = \frac{E}{\mu_{cell}} \quad (5.4)$$

Where E is the Young's Modulus of the cell. By using values of Young's moduli obtained from (Sokolov, 2007) and cell viscosity obtained from (Magraves, 2011), and normalizing it by the critical shear rate, a relaxation rate of 0.3996 was obtained and plotted over figure 5.6.

5.1.2 Backward Facing Step Case

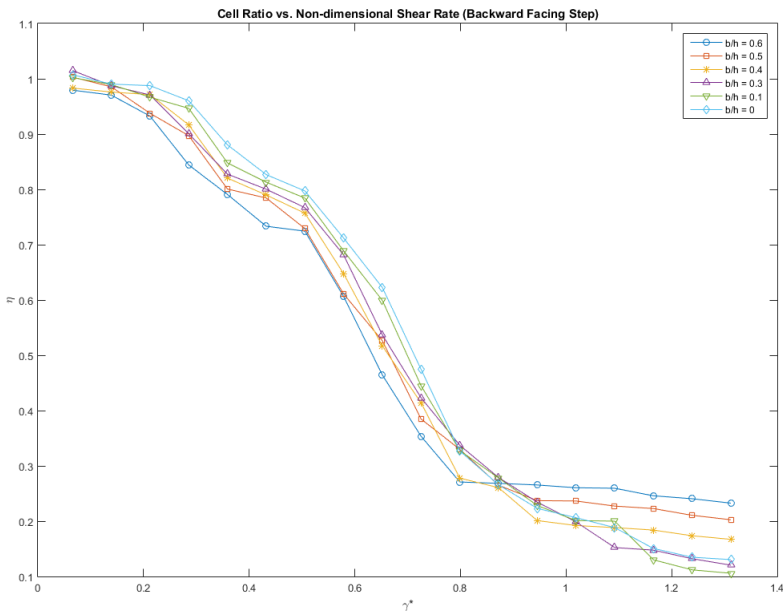


FIGURE 5.7: Plot of the Cell Ratio η vs. non-dimensional shear rate γ^* for different viscosities, μ for the backward facing step case

Another very interesting case to this research is how do specific morphologies perturb the results obtained in figure 5.4. The backward facing step morphology as discussed in Chapter 1 generates recirculation zones which may be preferential sites to cancer cell adhesion. Results of Chapter 4 show that within though there is higher average shear rate in the backward facing step morphology, there is marked lower shear stress in the regions of recirculation. As shown by bfs.cpp, Autodesk Inventor, the size of the recirculation zone increases with velocity.

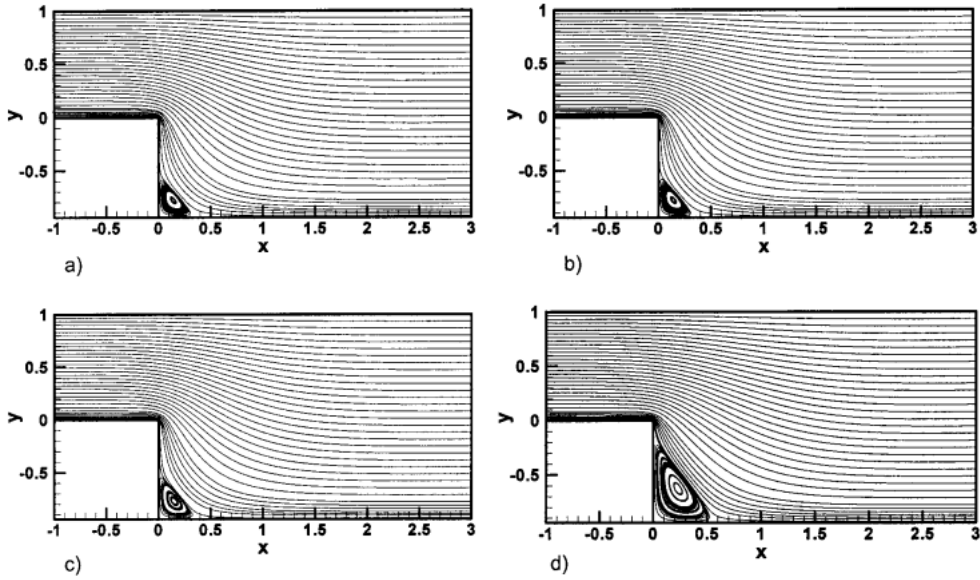


FIGURE 5.8: Flow in the vicinity of the step. (a) $Re = 0.0001$, (b) $Re = 0.1$, (c) $Re = 10$, (d) $Re = 50$. Adopted from (G. Biswas, 2004)

Also the size expansion ratio influences the size of the recirculation zone. As seen in figure 5.7 , an increase in expansion ratio b/h results in the development of larger recirculation zones. These recirculation zones with their lower shear rates promote greater retention according to figure 5.7. This plot again of Cell Ratio vs non-dimensional shear rate differs from figure 5.4 because of the plateaux that seemingly forms as shear rates are increased. This implies a case where even with increased shear rates, a small number of cells are retained longer due to low-shear microenvironment created by the backward facing step's recirculation zone. Also, a greater percentage of cells seem to be retained with larger expansion ratio, which matches the results obtained in Chapter 4.

While figure 5.7 tells displays a lot about the physics within the system, a more detailed analysis can be carried out to support some of the claims being made here. One way is to obtain the derivative of the cell ratio (η) and plot it against the Non-dimensional shear stress(γ^*). By doing this we obtain a probability density function for the Cell Number for a given shear rate.

5.2 Stochastic Model

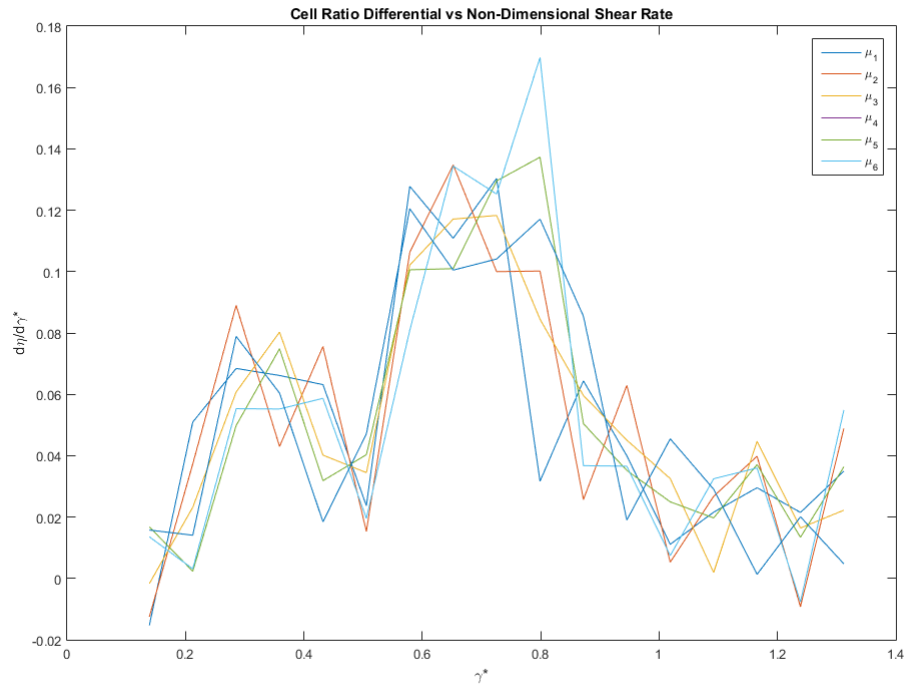


FIGURE 5.9: Plot of $\frac{d\eta}{d\gamma^*}$ for different viscosities, μ

Figure 5.9 agrees with some of the arguments made in Artem Efremov, 2011 of a bistability regime in shear-driven cell adhesion. From figure 5.9 we see two critical shear rates at which a significant change in cell number occur: γ_{*0} and γ_{*1} . In Efremov's paper they claim that in the stages of rolling adhesion, Selectins and their ligands provide initial bond formation to the walls by may permit rolling. This implies a weak field interaction, with dissociation stress τ_{c1} between the cell and the wall. Later on strong interaction, with dissociation stress τ_{c2} is achieved through the presence of Integrins whch results in stationary, firm or tight adhesion. The trends in the data seem to imply this by showing that at a lower shear rate regime γ_{*0} some portion of cells may be removed. These cells may have established majority Selectin linkages with the PDMS substrate and thus lacked the stiff linkage required to resist the lower shear stresses. However, the majority of cells may have already established strong linkages with the PDMS and required a higher shear stress γ_{*1} or greater to become detached.

Seeing this behavior, a stochastic model may be developed which takes advantage of the probability density function presented in figure 5.7. By fitting the data to a double Gaussian function of the form:

$$f(\gamma^*, \bar{\gamma}^*, \sigma) = Ae^{-\frac{(\gamma^* - \bar{\gamma}^*)^2}{2\sigma_1^2}} + Be^{-\frac{(\gamma^* - \bar{\gamma}^*)^2}{2\sigma_2^2}} \quad (5.5)$$

where $\bar{\gamma}^*_i$ represents the respective means and σ_1 is the standard deviation of the Gaussian functions. Using the curve-fitting toolbox in MATLAB, suitable values of the aforementioned parameters and A and B were obtained to generate the plot below.

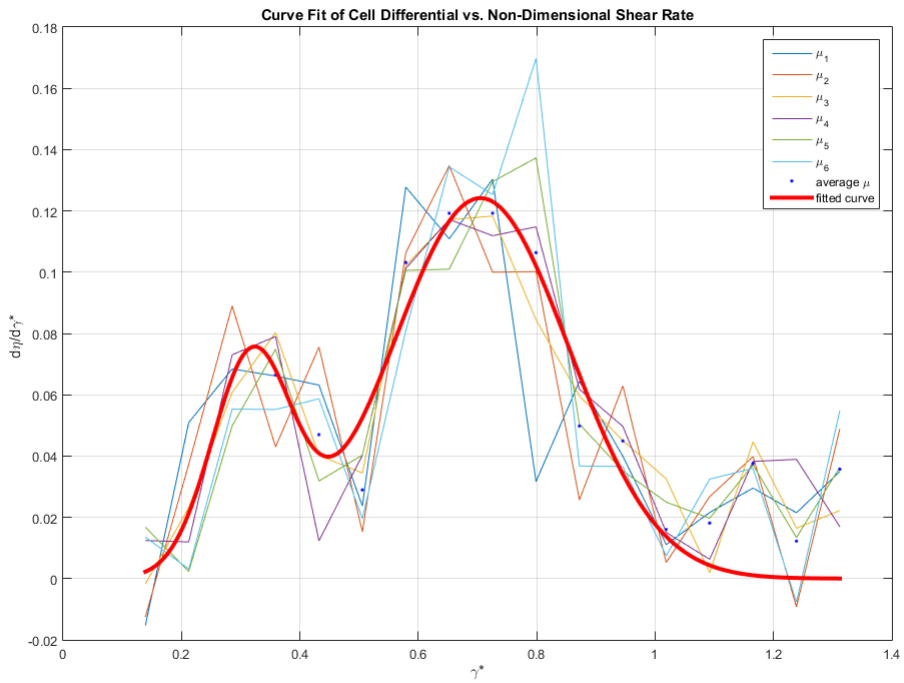


FIGURE 5.10: Plot of $\frac{d\eta}{d\gamma^*}$ for different viscosities, μ with fitted double-Gaussian curve. Mean of 0.7255 with Standard Deviation of 0.3702

From the Gaussian fit of the data, a smooth description of the probability density function is obtained and it can be now used to determine the cell ratio as a function of shear rate.

$$\eta(\gamma^*) = \int_{\gamma_0^*}^{\gamma_i^*} \left(Ae^{-\frac{(\gamma^* - \bar{\gamma}_1^*)^2}{2\sigma_1^2}} + Be^{-\frac{(\gamma^* - \bar{\gamma}_2^*)^2}{2\sigma_2^2}} \right) d\gamma^* \quad (5.6)$$

With an analytical solution of:

$$\eta(\gamma^*) = -A\sigma_1 \sqrt{\frac{\pi}{2}} \operatorname{erf} \left(\frac{\bar{\gamma}_1^* - \gamma^*}{\sigma_1} \right) - B\sigma_2 \sqrt{\frac{\pi}{2}} \operatorname{erf} \left(\frac{\bar{\gamma}_2^* - \gamma^*}{\sigma_2} \right) \quad (5.7)$$

Using this result, we can then extract from the numerically computed velocity field of the backward facing step, the expected cell ratio η given the shear rates in the domain. This was determined below for a case of Reynolds Number 1.

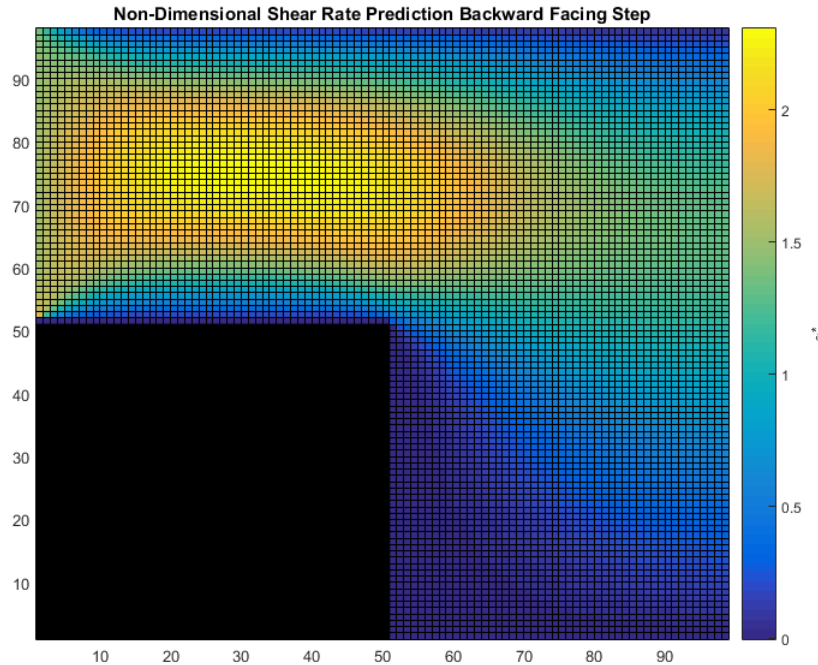


FIGURE 5.11: Shear Rate Prediction for $\text{Re} = 1$.

Using the shear rate data acquired from the simulation, we can easily extract η predictions by numerically integrating equation 5.4 over the entire domain.

Repeating this for a variety of initial conditions in the range of Reynolds Numbers of Interests, a plot of predicted trend in cell ratio was plotted on figure 5.6 to compare the accuracy of the method to experimental results for $b/h = 0.5$ and viscosity = μ_1 . This gave a plot that had a maximum error when compared to experimental results of 34%.

The discrepancy, overly conservative nature of the model may be linked to

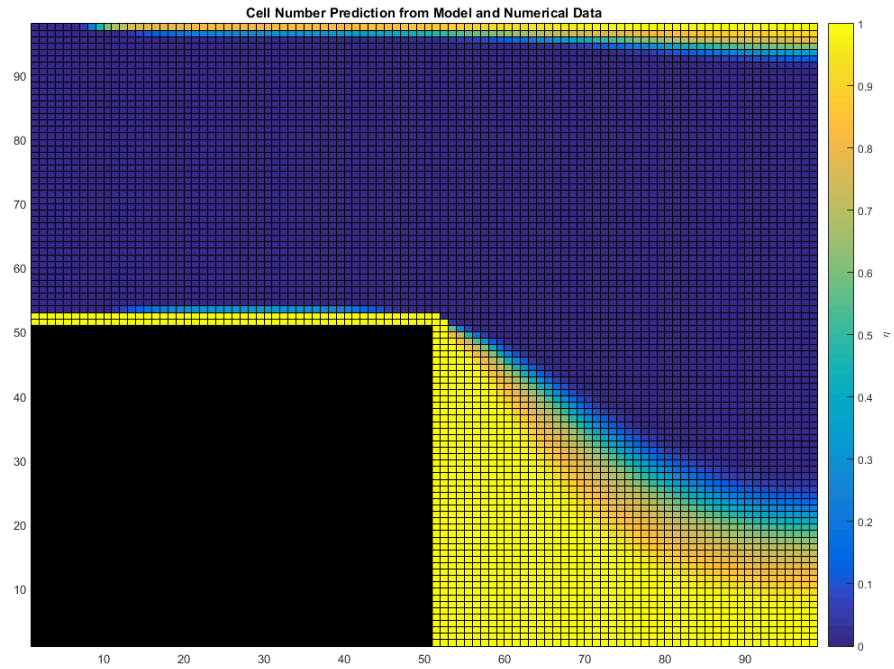


FIGURE 5.12: Corresponding η prediction using figure 5.10 and equation 5.5

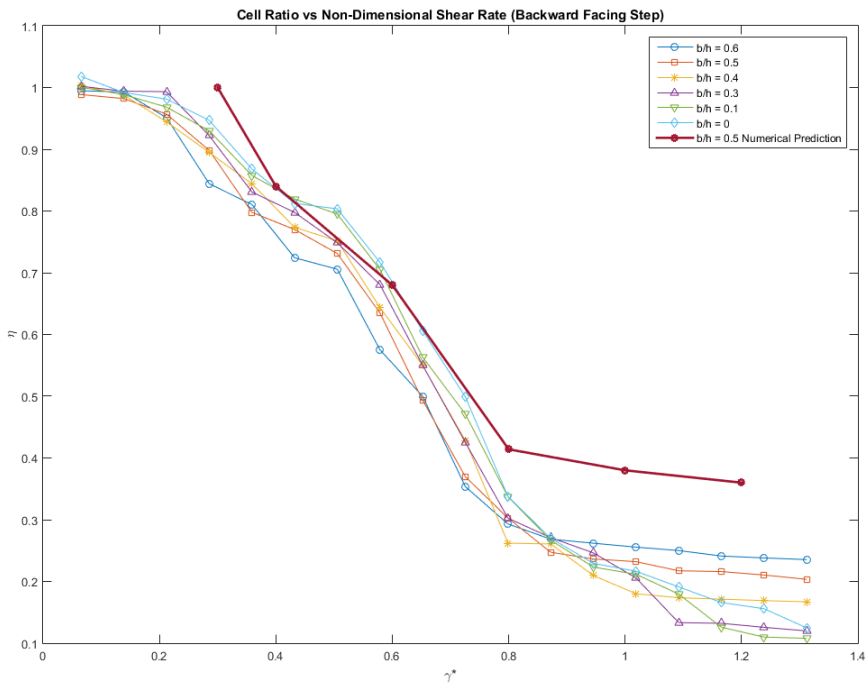


FIGURE 5.13: Predicted Adhesion as a function of Shear Rate using Model and Numerical Simulation

the models stochastic nature. Since this is modeled off datasets, this model may be improved by taking more data and obtain a more accurate Gaussian function to describe the adhesion behavior. Errors in the fidelity of the computation model may also hinder the prediction as the mesh could have been too coarse, or there may not have been enough nodal points in order to accurately simulate the real-world case. Also, we must not discount errors in the datasets as well. It is possible that some cells peeled off due to cell death and not due purely to shear giving an incorrect cell count. Though 3 trials at each shear rate was done, perhaps many more trials would be required in order to make this experiment more robust and the model more accurate.

Chapter 6

Conclusion

6.1 Experimental and Numerical Conclusions

The results of this experimental and numerical studies are not clear cut but they offer great insight into the relationship between cell adhesion and fluid mechanics. Firstly, they show that there exists a strong relationship between cell adhesion and shear rate. While shear stress, counter to the hypothesis, may not necessarily be a dominating factor in cancer cell adhesion – this can be explained through the strong role that shear rate plays in the dynamics and statics of the system.

The relationship between cell ratio and non-dimensional shear rate may be described with a Gaussian function with a confidence interval of 96%. When this model is coupled with the computational study, this model predicts the trends in cell adhesion with an accuracy that yielded a maximum error of 34% when compared to experimental results.

6.1.1 Ways to Improve the Numerics

The numerical simulations of used in this thesis could be improved by using more efficient or accurate numerical schemes in to discretize and solve the momentum equation. This could be done with the following suggestions:

1. Using a more accurate time advancing scheme such as Runga-Kutta in order to obtain a better solution in time,

2. The use of a pressure Poisson could be employed to solve the elliptic equation involving pressure (eliminated in our case due to form of the momentum equation we chose to solve). This would eliminate the difficulties with boundary conditions on vorticity and allow the simulation to be extended in three dimensions
3. If executed on a more powerful computational system, the size of the domain could be increased significantly and with a finer mesh in order to obtain a more accurate solution.
4. Other solvers could be investigated to further validate the solution such as finite volume methods.

6.1.2 Ways to Improve Experiments

There are many ways to improve the experiments that would have been considered if time was not a limiting factor. These factors center primarily around the experimental setup:

1. Using more cancer cells per trial to ensure that convergence behavior is not due to insufficient cell number.
2. Repeat the experiment many more times and averaging over large data sets to minimize the occurrence of random error and generate an improved representation of the relationship between.
3. Placing nutrient in the medium to which cells are exposed to could lower the chance of cell death.
4. Perhaps using a different polymer substrate than PDMS (such as endothelial cells on PDMS) to represent the biological environment of the blood vessel could yield interesting results.
5. Directly fitting an erf function to the dataset rather than a Gaussian to the derivative of the data may lead to a more accurate model in the future.

6.2 Suggestions for Future Work

Future work in this experiment is broad but the author suggests the following options:

1. Extending this argument to the use of non-Newtonian fluids. Blood is a complex non-Newtonian fluid and in order to capture the physics of the real biological interaction between the fluid forces that blood exerts on cancer cells, non-Newtonian models need to be developed.
2. Applying these models directly into Computational Models to examine the problem in greater detail than experiments may permit.
3. Using different types of cancer cells to verify if the behavior observed was unique or degenerate.
4. Constructing a model of a smooth profile backward facing to more closely represent the morphology of the blood vessels of interest.

Bibliography

- Alberts, B (2002). "Molecular biology of the cell". In: *Garland Science* 12, pp. 267–273.
- Artem Efremov, Jianshu Cao (2011). "Bistability of Cell Adhesion in Shear Flow". In: *Biophysical Journal* 101, pp. 1032–.
- Auerheimer J.; Kessler, H. (2006). "Bioorganic and Medicinal Chemistry Letter". In: *Annual Review of Cell Biology* 16, pp. 271–273.
- Bellomo N Li NK, Maini PK (2008). "On the foundations of cancer modelling: selected topics, speculations, and perspectives". In: *Math Models Methods Appl Sci* 18, 593–646.
- Biswas Abhijit, Manivannan M (2015). "Multiscale Layered Biomechanical Model of Pacinian Corpuscle". In: *IEEE Transactions of HAptics* 8, pp. 31–42.
- Bowers V.M., et. al (1989). "Cancer Cell Dynamics in Situ". In: *Journal of Biomedical Materials Research* 23, pp. 1453 –1473.
- Burridge K.; Fath, K.; Kelly T.; Nuckolls G.; Turner C. (1988). In: *Annual Review of Cell Biology* 4, pp. 487–525.
- Chambers A Groom A, MacDonald I. (2002). "Dissemination and growth of cancer cells in metastatic sites." In: *Nat. Rev. Cancer* 2, 563–72.
- Chu L.; Tempelman, L. A.; Miller C.; Hammer D. A (1994). "Cell Mechanics and Cellular Engineering Methods". In: *Aiche Journal* 40, pp. 692–703.
- Collins W., Shibeshi S. (2005). "The Rheology of Blood Flow in a Branched Arterial System". In: *Applied Rheology* 15, pp. 398–405.
- Disease Control, Centers for and Prevention (2015). *Cancer Facts*. URL: <http://www.cdc.gov/chronicdisease/resources/publications/aag/dcpc.htm> (visited on 2015).

- Erbertseder K Reichold J, Flemisch B Jenny P Helmig R (2012). "A coupled discrete/continuum model for describing cancer-therapeutic transport in the lung." In: *PLoS One* 7, pp. 3196 –.
- Fedosov DA Fornleitner J, Gompper G (2012). "Margination of white blood cells in microcapillary flow." In: *Phys Rev Lett.* 109, 7630–8104.
- Friedl P, Wolf K (2003a). "Tumour-cell invasion and migration: diversity and escape mechanisms." In: *Nat Rev Cancer* 3, 362–374.
- Friedl P, Wolf K. (2003b). "Tumour-cell invasion and migration: diversity and escape mechanisms". In: *Nat.Rev.Cancer* 3, 362–74.
- Fu, Gouguang (2019). "Drug Delivery Using Thermo-Responsive Poly (N-isopropylacrylamide) Based Hydrogel and Human Osteo-Sarcoma (HOS) Cell Adhesion on Biomaterials". In: *PhD Thesis* 1.
- G. Biswas M. Breuer, F. Durst (2004). "Backward-Facing Step Flows for Various Expansion Ratios at Low and Moderate Reynolds Numbers." In: *ASME* 126, pp. 362–372.
- Gossett DR Tse HTK, Lee SA Ying Y Lindgren AG et al (2012). "Hydrodynamic stretching of single cells for large population mechanical phenotypin". In: *Proc Nat Acad Sci USA* 109, 7630–7635.
- Graner F, Glazier JA (1992). "Simulation of biological cell sorting using a two-dimensional extended Potts model". In: *Phys Rev Lett.* 69, 2013–2016.
- Graziano L, Preziosi L (2007). "Mechanics in tumour growth. In: Mollica F, Rajagopal KR, Preziosi L (eds) Modeling of biological materials." In: *J Math Biol.* 43, 291–312.
- Griffin M. A.; Engler, A. J.; Barber T. A.; Healy K. E.; Sweeney H. L.; Discher D. (2004). "Patterning, prestress, and peeling dynamics of myocytes." In: *Biophysics Journal* 86, pp. 1209–1222.
- Guo L. Q.; Wang, R.; Xu H. M.; Liang J. (2006). "Application of ionic liquids for elution of bioactive flavonoid glycosides from lime fruit by miniaturized matrix solid-phase dispersion." In: *Chinese Journal of Analytical Chemistry* 34, pp. 359–361.
- Gupta GP, Massague J. (2006). "Cancer metastasis: building a framework". In: *Cell* 127, 679–95.

- Hammer DA, Lauffenburger DA (1989). "A dynamical model for receptor-mediated cell adhesion to surfaces in viscous shear flow." In: *Cell Biophysics* 14, pp. 138–173.
- Hanahan D, Weinberg RA. (2011). "Hallmarks of cancer: the next generation." In: *Cell* 144, 646–74.
- Huan W.; Anvari, B.; Torres J. H.; LeBaron R. G.; Athanasiou K. A. In: *Journal of Orthopaedic Research*.
- I.J., Fidler (2003). "The pathogenesis of cancer metastasis : the 'seed and soil' hypothesis revisited". In: *Nat.Rev.Cancer* 3, 453–58.
- Labelle (2011). "Direct signaling between platelets and cancer cells induces an epithelial mesenchymal-like transition and promotes metastasis." In: *Cancer Cell* 20, 576–90.
- Magraves, Charles (2011). "Atomic Force Microscopy in Cancer cell Research". In: *Bioengineering and Biotechnology* 108.10, pp. 2504–2508.
- MB, Sporn (1996). "The war on cancer." In: *Lancet* 347, 1377–1381.
- Meng S Tripathy D, Shete S Ashfaq R Haley B et al. (2004). "HER-2 gene amplification can be acquired as breast cancer progresses." In: *Natl. Acad. Sci.* 101, 9393–98.
- Mitchison T. J.; Cramer, L. P. (1996). In: *Cell* 84, pp. 371–379.
- Mrksich, M (2000). "Chemical Society Reviews". In: *Chemical Society Reviews* 29, pp. 267–273.
- Ozkaya (2012). "Fundamentals of Biomechanics:Equilibrium Motion and Deformation". In:
- Pivkin, Petros Koumoutsakos Igor (2013). "On the potency of Metastasis". In: p. 4.
- Polyak K, Weinberg RA. (2003). "Transitions between epithelial and mesenchymal states:acquisition of malignant and stem cell traits." In: *Nat.Rev.Cancer* 9, pp. 265–.
- PS., Steeg (2006). "Tumor metastasis: mechanistic insights and clinical challenges." In: *Nat. Med.* 12, 895–904.

- Rajasekaran, Jagannath (2011). "On the flow characteristics behind a backward-facing step and the design of a new axisymmetric model for their study". In: p. 4.
- Raucher D.; Sheetz, M.P (2000). "On Methods of Cell Measurement". In: *Journal of Cell Biology* 148, pp. 127–136.
- Resnick N Yahav H, Shay-Salit A Shushy M Schubert S et.al (2003). "Fluid shear stress and the vascular endothelium: for better and for worse." In: *Opt. Lett.* 81, 177–99.
- Ruoslahti E.; Obrink, B. (1996). "Experimental Cell Research". In: *Journal of Biomedical Materials Research* 227, pp. 1–11.
- Sarimollaoglu M Nedosekin D A, Simanovsky Y Galanzha E I Zharov V P. (2011). "In vivo photo acoustic time of flight velocity measurement of single cells and nanoparticles". In: *Opt. Letter.* 36, 4086–88.
- Senyah N.; Hildebrand, G.; Liefeth K. (2005). "Analytical and Bioanalytical Chemistry". In: *Annual Review of Cell Biology* 383, pp. 758–762.
- Sherratt JA, Chaplain MAJ (2001). "A new mathematical model for avascular tumour growth". In: *J Math Biol.* 43, 267–328.
- Small J. V.; Anderson, K.; Rottner K. (1996). In: *Biosci Rep* 16, pp. 351–368.
- Sokolov, Igor (2007). "Atomic Force Microscopy in Cancer cell Research". In: *Cancer Nanotechnology* 71, pp. 1–17.
- Sokolowski S, Herrmann H. (1992). "Dynamic phase separation of a fluid mixture". In: *Europhys. Lett.* 18, pp. 415–.
- Stephanou A McDougall SR, Anderson ARA Chaplain MAJ (2006). "Mathematical modelling of the influence of blood rheological properties upon adaptive tumour-induced angiogenesis." In: *Math Comput Model* 44, 96–123.
- Struckhoff AP Vitko JR, Rana MK Davis CT Foderingham KE et al. (2010). "Dynamic regulation of ROCK in tumor cells controls CXCR4-driven adhesion events." In: *J. Cell Sci.* 123, 401–12.
- Styp-Rekowska B Hlushchuk R, Pries AR Djonov V (2011). "Intussusceptive angiogenesis: pillars against the blood flow." In: *Acta Physiol* 202, 213–223.

- Sugihara-Seki M, Fu BM (2005). "Blood flow and permeability in microvessels." In: *Fluid Dyn Res* 37, 82–132.
- Tannehill J Arden D, Anderson R (2011). "Computational Methods in Fluid Dynamics with Heat Transfer". In: Connecticut, USA: CRC Press.
- Theodoros G.P., et al. (2005). "Vascular Wall Shear Stress: Basic Principles and Methods". In: *Hellenic Journal of Cardiology* 46, pp. 9–15.
- Valastyan S, Weinberg, R.A. (2011). "Tumor metastasis: molecular insights and evolving paradigms". In: *Cell* 47, 275– 92.
- Weiss, L (1989). "Biomechanical interactions of cancer cells with the microvasculature during metastasis". In: *Cell Biophysics* 14, pp. 187–215.
- Weiss, Leonard (1992). "Biomechanical interactions of cancer cells with the microvasculature during hematogenous metastasis". In: *Cancer and Metastasis* 11, pp. 227 –233.
- Wirtz D Konstantopoulos K, Searson PC (2011). "The physics of cancer: the role of physical interactions and mechanical forces in metastasis". In: *Nat.Rev.Cancer* 11, 512–22.
- Zeidman I., Buss JM (1952). "Transpulmonary passage of tumor cell emboli." In: *Cancer Res* 12, pp. 731–733.
- Zhang X. H.; Moy, V. T (2003). "Dynamic adhesion of T lymphocytes to endothelial cells revealed by atomic force microscopy." In: *Biophysical Chemistry* 104, pp. 271–278.